Asteroid Thermophysical Modeling

5 authors, including:

Marco Delbo
University of Nice Sophia Antipolis
241 PUBLICATIONS   **2,183** CITATIONS

Michael Mueller
Hochschule Ravensburg-Weingarten
111 PUBLICATIONS   **950** CITATIONS

Some of the authors of this publication are also working on these related projects:

Project   PRIMitive Asteroids Spectroscopic Survey (PRIMASS) View project

Project   1st Gaia intermediate release: study its impact on ground-based asteroid astrometry. View project

Asteroid thermophysical modeling

Marco Delbo

Laboratoire Lagrange, UNS-CNRS, Observatoire de la Côte d'Azur

Michael Mueller

SRON Netherlands Institute for Space Research

Joshua P. Emery

Dept. of Earth and Planetary Sciences - University of Tennessee

Ben Rozitis

Dept. of Earth and Planetary Sciences - University of Tennessee

Maria Teresa Capria

Istituto di Astrofisica e Planetologia Spaziali, INAF

The field of asteroid thermophysical modeling has experienced an extraordinary growth in the last ten years, as new thermal infrared data became available for hundreds of thousands of asteroids. The infrared emission of asteroids depends on the body's size, shape, albedo, thermal inertia, roughness and rotational properties. These parameters can therefore be derived by thermophysical modeling of infrared data. Thermophysical modeling led to asteroid size estimates that were confirmed at the few-percent level by later spacecraft visits. We discuss how instrumentation advances now allow mid-infrared interferometric observations as well as high-accuracy spectro-photometry, posing their own set of thermal-modeling challenges. We present major breakthroughs achieved in studies of the thermal inertia, a sensitive indicator for the nature of asteroids soils, allowing us, for instance, to determine the grain size of asteroidal regoliths. Thermal inertia also governs non-gravitational effects on asteroid orbits, requiring thermophysical modeling for precise asteroid dynamical studies. The radiative heating of asteroids, meteoroids, and comets from the Sun also governs the thermal stress in surface material; only recently has it been recognized as a significant weathering process. Asteroid space missions with thermal infrared instruments are currently undergoing study at all major space agencies. This will require a high level of sophistication of thermophysical models in order to analyze high-quality spacecraft data.

1. INTRODUCTION

Asteroid thermophysical modeling is about calculating the temperature of asteroids' surface and immediate sub-surface, which depend on absorption of sunlight, multiple scattering of reflected and thermally emitted photons, and heat conduction. Physical parameters such as albedo (or reflectivity), thermal conductivity, heat capacity, emissivity, density and roughness, along with the shape (e.g., elevation model) of the body, its orientation in space, and its previous thermal history are taken into account. From the synthetic surface temperatures, thermally emitted fluxes (typically in the infrared) can be calculated. Physical properties are constrained by fitting model fluxes to observational data.

One differentiates between sophisticated *thermophysical models* (*TPMs;* Lebofsky and Spencer, 1989; Spencer, 1990; Spencer et al., 1989; Lagerros, 1997, 1996a, 1998; Delbo, 2004; Mueller, 2007; Rozitis and Green, 2011) and *simple thermal models*, which typically assume spherical shape, neglect heat conduction (or simplify its treatment), and do not treat surface roughness (see Harris and Lagerros, 2002; Delbo and Harris, 2002, for reviews). In the past, usage of TPMs was reserved to the few exceptional asteroids for which detailed shape models and high quality thermal infrared data existed (Harris and Lagerros, 2002). In the last ten years, however, TPMs became significantly more applicable (see § 6), thanks both to new spaceborn infrared telescopes (*Spitzer*, *WISE* and *AKARI;* see Mainzer et al., 2015) and to the availability of an ever-growing number of asteroid shape models (Durech et al., 2015).

After introducing the motivations and the different contexts for calculating asteroid temperatures (§ 2), we provide an overview of simple thermal models (§ 3) and of TPMs (§ 4). We describe data analysis techniques based on TPMs (§ 5), then we present the latest results and implications on the physics of asteroids (§ 6). In § 7, we discuss temperature-induced surface changes on asteroids; see

also the chapter "Asteroid surface geophysics" by Murdoch et al. (2015). All used symbols are summarized in Tab. 1.

Note that we do not discuss here the so-called asteroid *thermal evolution models* that are generally used to compute the temperature throughout the body as a function of time, typically taking into account internal heat sources such as the decay of the radiogenic ^{26}Al. Such models allow one to estimate the degree of metamorphism, aqueous alteration, melting and differentiation that asteroids experienced during the early phases of the solar system formation (see McSween et al., 2002, for a review).

2. MOTIVATIONS AND APPLICATIONS OF TPMs

Thermophysical modeling of observations of asteroids in the thermal infrared ($\lambda \gtrsim 4~\mu$m) is a powerful technique to determine the values of physical parameters of asteroids such as their sizes (e.g., Müller et al., 2014a), the thermal inertia and the roughness of their soils (e.g., Müller and Lagerros, 1998; Mueller, 2007; Delbo and Tanga, 2009; Matter et al., 2011; Rozitis and Green, 2014; Capria et al., 2014) and in some particular cases also of their bulk density and their bulk porosity (Rozitis et al., 2013, 2014; Emery et al., 2014; Chesley et al., 2014)

Knowledge of physical properties is crucial to understand asteroids: for instance, size information is fundamental to constrain the asteroid size frequency distribution that informs us about the collisional evolution of these bodies (Bottke et al., 2005); is paramount for the study of asteroid families, for the Earth-impact risk assessment of near-Earth asteroids (NEAs; see Harris et al., 2015, for a review), and for the development of asteroid space mission scenarios (§ 5.7). Accurate sizes are also a prerequisite to calculate the volumes of asteroids for which we know the mass, allowing us to derive the bulk density, which inform us about the internal structure of these bodies (e.g., Carry, 2012).

Thermal inertia, the resistance of a material to temperature change (§ 5.2), is a sensitive indicator for the properties of the grainy soil (regolith, Murdoch et al., 2015) on asteroids, e.g., the typical grain size (Gundlach and Blum, 2013) and their degree of cementation (Piqueux and Christensen, 2009a,b) can be inferred from thermal-inertia measurements. In general, the regolith is what we study by means of remote-sensing observations. Understanding the regolith is therefore crucial to infer the nature of the underlying body. Regolith informs us about the geological processes occurring on asteroids (Murdoch et al., 2015) such as impacts, micrometeoroid bombardment (Hörz and Cintala, 1997), and thermal cracking (Delbo et al., 2014). Regolith contains records of elements implanted by the solar wind and cosmic radiation, and therefore informs us about the sources of those materials (Lucey, 2006). Regolith porosity can shed light on the role of electrostatic and van-der-Waals forces acting on the surface of these bodies (e.g., Rozitis et al., 2014; Vernazza et al., 2012).

Knowledge of surface temperatures is also essential for the design of the instruments and for the near-surface operation of space missions, as in the case of the sample-return missions Hayabusa-II and OSIRIS-REx of JAXA and NASA, respectively, In the future, knowledge of asteroid temperatures will be crucial for planning human interaction with asteroids.

Another reason to model asteroid surface temperatures is that they affect its orbital and spin state evolution via the Yarkovsky and YORP effects, respectively (§ 5.8 and Vokrouhlický et al., 2015). In particular, thermal inertia dictates the strength of the asteroid Yarkovsky effect. This influences the dispersion of members of asteroid families, the orbital evolution of potentially hazardous asteroids, and the delivery of $D \lesssim 40$ km asteroids and meteoroids from the main belt into dynamical resonance zones capable of transporting them to Earth-crossing orbits (see Vokrouhlický et al., 2015, and the references therein).

The YORP effect is believed to be shaping the distribution of rotation rates (Bottke et al., 2006) and spin vector orientation (Vokrouhlický et al., 2003; Hanuš et al., 2011, 2013); small gravitationally bound aggregates could be spun up so fast (Vokrouhlický et al., 2015; Bottke et al., 2006, and references therein) that they are forced to change shape and/or undergo mass shedding (Holsapple, 2010). Approximately 15% of near-Earth asteroids are observed to be binaries (Pravec et al., 2006), and YORP spin up is proposed as a viable formation mechanism (Walsh et al., 2008; Scheeres, 2007; Jacobson and Scheeres, 2011).

A further motivation to apply TPM techniques is to constrain the spin-axis orientation and the sense of rotation of asteroids (examples are 101955 Bennu and 2005 YU$_{55}$, Müller et al., 2012, 2013). Durech et al. (2015) describe how to use optical and thermal infrared data simultaneously to derive more reliable asteroid shapes and spin properties.

The temperature and its evolution through the entire life of an asteroid can alter its surface composition and nature of the regolith (§ 7). For example, when the temperature rises above a certain threshold for a sustained period, certain volatiles can be lost via sublimation (Schorghofer, 2008; Capria et al., 2012), dehydration (Marchi et al., 2009), or desiccation (Delbo and Michel, 2011; Jewitt et al., 2015, and references therein).

There can be pronounced and fast temperature variations between day and night. Modeling these temperature variations is fundamental to studying the effect of thermal cracking of asteroid surface material (§ 7.1), which was found to be an important source of fresh regolith production (Delbo et al., 2014).

3. SIMPLE THERMAL MODELS

We start by introducing the near-Earth asteroid thermal model (NEATM, Harris, 1998) that is typically used where the data quality and/or the available knowledge about asteroid shape and spin preclude the usage of TPMs. Typically, the NEATM allows a robust estimation of asteroid diameter and albedo, but does not provide any direct information on thermal inertia or surface roughness (see Harris

and Lagerros, 2002, for a review). The recent large-scale thermal-emission surveys of asteroids and trans-Neptunian objects (see Mainzer et al., 2015; Lellouch et al., 2013, and references therein) typically use the NEATM in their data analysis, thereby establishing it as the de-facto default among the simple thermal models. The typical NEATM accuracy is 15% in diameter and roughly 30% in albedo (Harris, 2006). Other simple thermal models are the "Standard Thermal Model" (STM; Lebofsky et al., 1986), the "Isothermal Latitude Model" (ILM, also known as the Fast Rotating Model or FRM, Lebofsky and Spencer, 1989), and the night emission simulated thermal model (NESTM by Wolters and Green, 2009). The STM and the ILM, reviewed by, e.g., Harris and Lagerros (2002), have largely fallen out of use.

The NEATM assumes that the asteroid has a spherical shape and does not directly account for thermal inertia nor surface roughness. The surface temperature is given by the instantaneous equilibrium with the insolation, which is proportional to the cosine of the angular distance between local zenith and the Sun and zero at the night side. The maximum temperature occurs at the subsolar point and it reads:

$$(1 - A)S_\odot r^{-2} = \eta \sigma \epsilon \, T_{\text{SS}}^4 \qquad (1)$$

(nomenclature is provided in Tab. 1). The parameter η was introduced in the STM of Lebofsky et al. (1986) as a means of changing the model temperature distribution to take account of the observed enhancement of thermal emission at small solar phase angles due to surface roughness. This is known as the beaming effect. For this reason η is also called the *beaming parameter*. The η formalism, in the NEATM, allows a first-order description of the effect of a number of geometrical and physical parameters, in particular the thermal inertia and surface roughness on the spectral energy distribution of an asteroid (Delbo et al., 2007). For a large thermal inertia, one would expect η-values significantly larger than unity (e.g., 1.5–3; with theoretical maximum values around 3.5; Delbo et al., 2007), whereas for low thermal inertia $\eta \simeq 1$ (for $\Gamma = 0$ and zero surface roughness). Roughness, on the other hand, tends to lower the value of η (for observations at low or moderate phase angles). For instance, a value of $\eta \sim 0.8$ for a main belt asteroid indicates that this body has low thermal inertia and significant roughness (with minimum theoretical values of 0.6 - 0.7; Spencer, 1990; Delbo et al., 2007). We note, however, that η is not a physical property of an asteroid, as it can vary due to changing observing and illumination geometry, aspect angle, heliocentric distance of the body, phase angle and wavelength of observation.

4. THERMOPHYSICAL MODELS

4.1. Overview

Different TPMs have been proposed to study the thermal emission of asteroids, comets, planets, and satellites. The first models were motivated by thermal observations of the lunar surface, which revealed an almost thermally insulating surface that emitted thermal radiation in a non-Lambertian way (Pettit and Nicholson, 1930; Wesselink, 1948a). Heat conduction and radiation scattering models of various rough surfaces were able to reproduce the lunar observations to a good degree (e.g., Smith, 1967; Buhl et al., 1968b,a; Sexl et al., 1971; Winter and Krupp, 1971), and the derived thermal inertia and surface roughness values matched *in situ* measurements by Apollo astronauts (see Rozitis and Green, 2011, and references therein). These early lunar models were adapted to general planetary bodies, albeit with an assumed spherical shape, by Spencer et al. (1989) and Spencer (1990). The most commonly used asteroid TPMs of Lagerros (1996a, 1997, 1998), Delbo (2004), Mueller (2007), and Rozitis and Green (2011) are all based on Spencer et al. (1989) and Spencer (1990). Here we present the basic principles utilized in TPMs; for implementation details, the reader is referred to the quoted works.

All TPMs represent the global asteroid shape as a mesh of (triangular) facets (see Fig. 1) that rotates around a given spin vector with rotation period P. In general, utilized shape models are derived from radar observations, inversion of optical light-curves, in-situ spacecraft images, or stellar occultation timing (see Durech et al., 2015, for a review of asteroid shape modeling). If no shape model is available, one typically falls back to a sphere or an ellipsoid (e.g., Müller et al., 2013, 2014a; Emery et al., 2014).

The goal is to calculate the thermal emission of each facet of the shape model at a given illumination and observation geometry. To this end, the temperature of the surface and, in the presence of thermal inertia, the immediate subsurface need to be calculated. Generally, lateral heat conduction can be neglected as the shape model facets are much larger than the penetration depth of the diurnal heat wave (i.e., the thermal skin depth), and only 1D heat conduction perpendicular to and into the surface needs to be considered. For temperature T, time t, and depth z, 1D heat conduction is described by:

$$\rho C \frac{\partial T}{\partial t} = \frac{\partial}{\partial z} \kappa \frac{\partial T}{\partial z} \qquad (2)$$

where κ is the thermal conductivity, ρ is the material density, and C is the heat capacity. If κ is independent of depth (and, implicitly, temperature independent, see §5.3), Eq. 2 reduces to the diffusion equation:

$$\frac{\partial T}{\partial t} = \frac{\kappa}{\rho C} \frac{\partial T^2}{\partial^2 z} \qquad (3)$$

It is useful to define the thermal inertia Γ and the thermal skin depth l_s

$$\Gamma = \sqrt{\kappa \rho C} \qquad (4)$$

$$l_s = \sqrt{\kappa P / 2\pi \rho C}. \qquad (5)$$

These material properties are generally assumed to be constant with depth and temperature in asteroid TPMs, but varying properties has been considered in some Moon, Mars, planetary satellites, and asteroids models (e.g Giese

TABLE 1

NOMENCLATURE

Symbol	Quantity	Unit		Symbol	Quantity	Unit
T	Temperature	K		$\bar{\theta}$	Mean surface slope	deg
T_{SS}	Subsolar temperature	K		l_s	Thermal skin depth	m
σ	Stefan-Boltzmann constant	$(5.67051\ 10^{-8})$ W m^{-2} K^{-4}		P	Rotation period	s
$S_\odot$	Solar constant at $r=1$ au	(1329) W m^{-1}		ω	$=2\pi/P$	s^{-1}
r	Distance to the Sun	au		λ_p	ecliptic longitude of the pole	deg
$\vec{r}$	Vector to the Sun	m		β_p	ecliptic latitude of the pole	deg
Δ	Distance to the observer	au		ϕ_0	Initial rotational phase at epoch	deg
ϵ	Emissivity	-		α	(Phase) angle between asteroid-sun-observer	deg
η	Beaming parameter	-		a	Area of a facet	m^2
κ	Thermal conductivity	W m^{-1} K^{-1}		S	Shadowing function	
C	Heat capacity	J kg^{-1} K^{-1}		$F_{\vec{\imath},\vec{\jmath}}$	View factor	
Γ	Thermal inertia	J m^{-2}s$^{-1/2}$K^{-1}		$J_V(\vec{\jmath})$	Visible radiosity	
Θ	Thermal parameter	-		$J_{IR}(\vec{\jmath})$	Infrared radiosity	
ρ	Material density	kg m^{-3}		$\hat{n}$	Local normal	m
H	Absolute magnitude of the H,G system			$\vec{\imath}$	Vector to the local facet	m
G	Slope parameter of the H,G system			$\vec{\jmath}$	Vector to the remote facet	m
V	Actual magnitude in the V-band			γ_C	Crater opening angle	deg
D	Diameter	m (or km)		ρ_C or f	Area density of craters	
A	Bolometric Bond albedo	-		ϕ	Emission angle	rad
p_V	Geometric visible albedo	-		$f_\lambda(\tau)$	Infrared flux	W m^{-2} μm^{-1}
z	Depth in the subsoil	m		λ	Wavelength	μm
t	Time	s				
r_p	Pore radius of regolith	m				

and Kuehrt, 1990; Urquhart and Jakosky, 1997; Piqueux and Christensen, 2011; Keihm, 1984; Keihm et al., 2012; Capria et al., 2014, see also section 5.3).

TPM implementations typically employ dimensionless time and depth variables: $\tau = 2\pi t/P$ and $Z = z/l_s$. Then, the only remaining free parameter is the dimensionless thermal parameter ($\Theta = \Gamma\sqrt{\omega}/\epsilon\sigma T_{SS}^3$, Spencer, 1990) describing the combined effect of thermal inertia, rotation period, and heat emission into space on the surface temperature distribution (see Fig. 2).

A numerical finite-difference technique is used to solve the 1D heat conduction equation, and an iterative technique is used to solve the surface boundary condition. This requires a suitable number of time and depth steps to fully resolve the temperature variations and to ensure model stability (typically, at least 360 time steps and 40 depth steps over 8 thermal skin depths are required). TPMs are run until specified convergence criteria are met (e.g., until temperature variations between successive model iterations are below a specified level) and/or until a specified number of model iterations have been made.

For applications such as the study of the sublimation of water ice from the shallow subsurface of asteroids (e.g., the *Main Belt Comets* or 24 Themis) the heat conduction equation must be coupled with a gas diffusion equation (Schorghofer, 2008; Capria et al., 2012; Prialnik and Rosenberg, 2009). See also Huebner et al. (2006) for a review.

The 1D heat conduction equation is solved with internal and surface boundary conditions to ensure conservation of energy. Since the amplitude of subsurface temperature variations decreases exponentially with depth, an internal boundary condition is required to give zero temperature gradient at a specified large depth

$$\left(\frac{\partial T}{\partial z}\right)_{z\gg l_s} = 0. \tag{6}$$

A typical surface boundary condition for a facet at point $\vec{\imath}$ with respect to the asteroid origin, at point $\vec{r}$ with respect to the Sun, and with surface normal $\hat{n}$ is then given by

$$\epsilon\sigma T^4(\vec{\imath},t) - \left(\frac{\partial T(\vec{\imath},t)}{\partial z}\right)_{z=0} =$$
$$\frac{(1-A)S_\odot}{\vec{r}^{\,3}}(\vec{r}\cdot\hat{n})(1-S(\vec{r},\vec{\imath}))+$$
$$(1-A)\int J_V(\vec{\jmath})F_{\vec{\imath},\vec{\jmath}}\,da'+$$
$$\epsilon\sigma(1-\epsilon)\int J_{IR}(\vec{\jmath})F_{\vec{\imath},\vec{\jmath}}\,da' \tag{7}$$

The left-hand side of Eq. (7) gives the thermal energy radiated to space and the heat conducted into the subsurface, and the right-hand side gives the input radiation from three different sources: direct solar radiation, multiply scattered solar radiation (i.e., self-illumination), and reabsorbed thermal radiation (i.e., self-irradiation). The two last components are also known as mutual heating (see Fig. 3).

The amount of solar radiation absorbed by a facet depends on the Bond albedo A and any shadows projected on it, which is dictated by $S(\vec{r},\vec{\imath})$ (i.e., $S(\vec{r},\vec{\imath}) = 1$ or 0, depending on the presence or absence of a shadow). Projected shadows occur on globally non-convex shapes only, which can be determined by ray-triangle intersection tests of the solar illumination ray (e.g., Rozitis and Green, 2011) or by local horizon mapping (e.g., Statler, 2009). Related to shadowing are the self-heating effects arising from interfacing
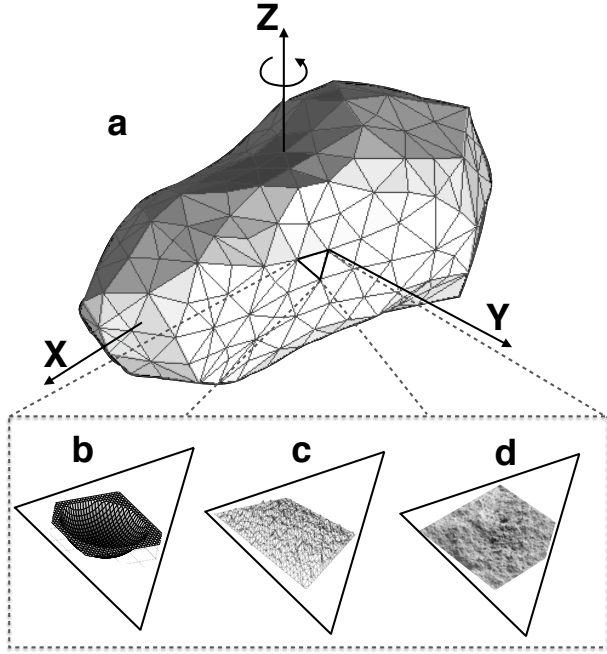
Fig. 1.— (a) example of a triangulated 3D shape model as typically used in TPMs (asteroid (2063) Bacchus from http://echo.jpl.nasa.gov/asteroids/shapes/shapes.html). Temperatures are color coded: white corresponds to the maximum and dark-gray corresponds to minimum temperature. Three different roughness models are sketched in the bottom of the figure: (b) hemispherical section craters; (c) Gaussian surface; (d) fractal surface. Sub-figures b and d are adapted from Davidsson et al. (2015), c is from Rozitis and Green (2011).

Fig. 2.— Synthetic diurnal temperature curves on the equator of a model asteroid for different values of thermal inertia (in units of J m^{-2}s$^{-1/2}$K^{-1}). Increasing thermal inertia smooths temperature contrasts and causes the temperature peak to occur after the insolation peak at 3 h. The asteroid is situated at a heliocentric distance of r = 1.1 au, has a spin period of 6 h, a Bond albedo of A = 0.1, and its spin axis is perpendicular to the orbital plane.

facets, which tend to reduce the temperature contrast produced inside concavities. The problem here is to determine which facets see other facets, and to calculate the amount of radiation exchanged between them. The former can be determined by ray-triangle intersection tests again, and the latter can be solved using view factors. The view factor $F_{\vec{i},\vec{j}}$ is defined as the fraction of the radiative energy leaving the local facet $\vec{i}$ that is received by the remote facet $\vec{j}$ assuming Lambertian emission (Lagerros, 1998). $J_V(\vec{j})$ and $J_{IR}(\vec{j})$ are then the visible and thermal-infrared radiosities of remote facet $\vec{j}$. Either single or multiple scattering can be taken into account, and the latter can be efficiently solved using Gauss-Seidel iterations (Vasavada et al., 1999). Most TPMs neglect shadowing and self-heating effects resulting from the global shape for simplicity, but they can be significant on asteroids with large shape concavities (e.g., the south pole of (6489) Golevka: Rozitis and Green, 2013).

4.2. Modeling asteroid thermal emission

Once the surface temperature distribution across an asteroid surface has been computed, the emission spectrum (Fig. 4) at a given observation geometry and a specified time can be calculated. The monochromatic flux density can also be calculated at wavelengths of interest. When these model fluxes are pl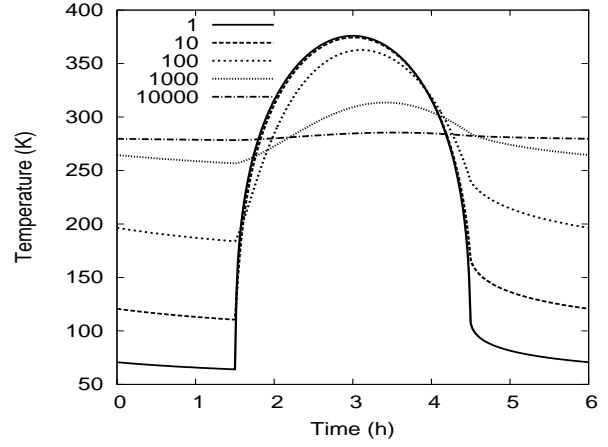otted as a function of the asteroid rotational phase, one obtains the so-called thermal lightcurves (e.g. Fig. 5), which can be used to test the fidelity of shape and albedo models typically used as input in the TPM.

When the temperature for a facet is known, the intensity $I_\lambda(\tau)$ at which it emits at wavelength λ is given by the Planck function. Assuming Lambertian emission, the spectral flux of the facet seen by an observer is then

$$f_\lambda(\tau) = I_\lambda(\tau)\frac{a}{\Delta^2}\cos\phi \qquad (8)$$

where a is area of the facet, Δ is the distance to the observer, and ϕ is the emission angle. The total observed flux is obtained by summing the thermal fluxes of all visible shape model facets including any contributions from surface roughness elements contained within them. For disk-integrated measurements, this summation is performed across the entire visible side of the asteroid, whilst for spatially resolved measurements it is summed across facets contained within the detector pixel's field of view.

The assumption of Lambertian emission depends on no directionality induced by surface irregularities at scales below the thermal skin depth. Davidsson and Rickman (2014) show that surface roughness at sub-thermal-skin-depth scales is quasi-isothermal and is therefore not likely to deviate from Lambertian emission overall. However, radiative transfer processes between the regolith grains could contribute up to 20% of the observed beaming effects (Hapke, 1996). Rozitis and Green (2011, 2012) investigated combined microscopic (regolith grain induced) and macroscopic (surface roughness induced) beaming effects, and demonstrated that the macroscopic effects dominated overall. This was previously found to be the case in directional thermal emission measurements of lava flows on Earth (Jakosky et al., 1990).
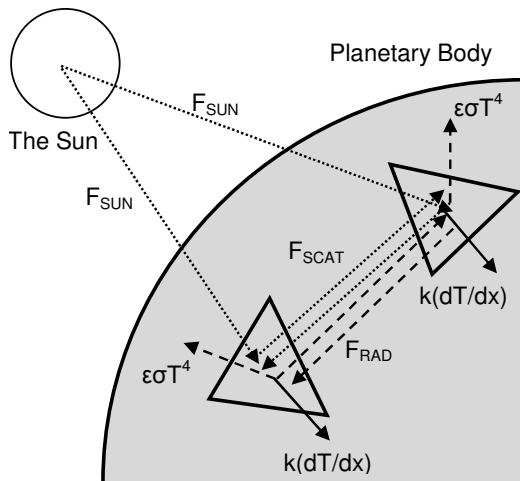
Fig. 3.— Diagram illustrating the energy balance and radiation transfer between facets (copied from Rozitis and Green, 2011). The terms F_{SUN}, F_{SCAT}, F_{RAD}, $k(dT/dx)$ and $\epsilon\sigma T^4$ are the direct sunlight, multiply scattered sunlight, reabsorbed thermal radiation, conducted heat and thermal radiation lost to space, respectively.
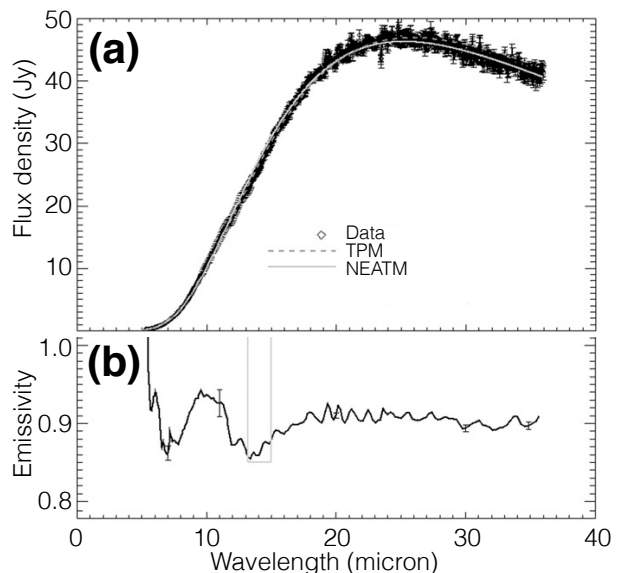

Fig. 4.— (a) Example of SED calculated from a TPM and the NEATM compared to a Spitzer spectrum of (87) Sylvia. (b) Spectral emissivity derived from the above: data divided by the NEATM continuum. Figure from Marchis et al. (2012).

As wavelengths increase to the submillimeter range and above, asteroid regolith becomes increasingly transparent and the observed flux is integrated over increasing depths (Chamberlain et al., 2009; Keihm et al., 2013). Modeling such fluxes with typical thermal models (which derive fluxes from surface temperatures, only) requires a significant reduction in effective spectral emissivity. For example, 3.2 mm flux measurements of (4) Vesta require an emissivity of ∼0.6 to match model predictions (Müller and Barnes, 2007). The reduction in emissivity can be explained by lower subsurface emission temperatures (Lagerros, 1996b) and by different subsurface scattering processes dependent on grain size (Redman et al., 1992; Müller and Lagerros, 1998). Keihm et al. (2012, 2013) attribute the reduced emissivity at submm/mm wavelengths to a higher thermal inertia value of the subsurface layers. Reduction in emissivity has also been determined at wavelengths shorter than 4.9 μm for disk-resolved regions of (4) Vesta (Tosi et al., 2014).

4.3. Surface Roughness

Roughness causes an asteroid surface to thermally emit in a non-Lambertian way with a tendency to reradiate the absorbed solar radiation back towards the Sun, an effect known as thermal infrared beaming (Lagerros, 1998; Rozitis and Green, 2011). It is thought to be the result of two different processes: a rough surface will have elements orientated towards the Sun that become significantly hotter than a flat surface, and multiple scattering of radiation between rough surface elements increases the total amount of solar radiation absorbed by the surface. The relevant size scale ranges from the thermal skin depth to the linear size of the facets in the shape model. It is included in thermophysical models by typically modeling an areal fractional coverage (f) of spherical-section craters (of opening angle γ_C) within each shape model facet. Other more complex forms have been considered, such as Gaussian random (Lagerros, 1998) or fractal (Groussin et al., 2013) surfaces or parallel sinusoidal trenches (see sketch of Fig. 1) , but the spherical-section crater produces similar results (in terms of the disk-integrated beaming effect Lagerros, 1998) and accurately reproduces the directionality of the lunar thermal infrared beaming effect (Rozitis and Green, 2011). However, it has been shown that the thermal emission depends also on roughness type in addition to roughness level, for disk resolved data Davidsson et al. (2015).

Spherical-section craters are typically implemented, as the required shadowing and view-factor calculations can be performed analytically (Emery et al., 1998; Lagerros, 1998). Heat conduction can be included by dividing the crater into several tens of surface elements where the same equations listed above can be applied. Alternatively, the temperature distribution within the crater resulting from heat conduction, $T_{\text{crater}}(\Gamma)$, can be approximated using

$$\frac{T_{\text{rough}}(\Gamma)}{T_{\text{rough}}(0)} = \frac{T_{\text{smooth}}(\Gamma)}{T_{\text{smooth}}(0)} \tag{9}$$

where $T_{\text{rough}}(0)$ can be calculated analytically assuming instantaneous equilibrium (Lagerros, 1998). $T_{\text{smooth}}(0)$ and $T_{\text{smooth}}(\Gamma)$ are the corresponding smooth-surface temperatures, which can be calculated exactly. This approximation is computationally much cheaper than the full implementation. However, it does not work on the night side of the asteroid and temperature ratios diverge near the terminator (Mueller, 2007). An even simpler alternative is to multiply the smooth-surface temperatures by a NEATM-like η
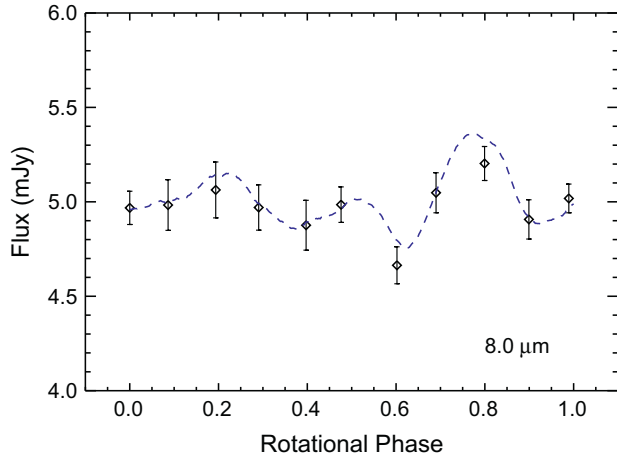
6

Fig. 5.— Example of a TPM generated thermal lightcurve (dashed line) and real data for (101955) Bennu. From Emery et al. (2014).

value (e.g. Groussin et al., 2011). Whilst this alternative might produce the correct disk-integrated color temperature of the asteroid, it does not reproduce the directionality of the beaming effect. Indeed, roughness models predict a limb-brightening effect (Rozitis and Green, 2011), which is seen in spatially-resolved measurements of (21) Lutetia by Rosetta (Keihm et al., 2012).

The above implementations neglect lateral heat conduction, although the spatial scales representing surface roughness can, in some cases, become comparable to the thermal skin depth. Modeling of 3D heat conduction inside rocks the size of the thermal skin depth has demonstrated that their western sides (for a prograde rotator; eastern sides for a retrograde rotator) are generally warmer than their eastern sides, which could result in a tangential-YORP effect that predominantly spins up asteroids (Golubov and Krugly, 2012). Other than this, it appears that the 1D heat conduction approximation still produces satisfactory results.

In thermophysical models, the degree of surface roughness can be quantified in terms of the Hapke mean surface slope

$$\tan \bar{\theta} = \frac{2}{\pi} \int_0^{\pi/2} a(\theta) \tan \theta \, d\theta \qquad (10)$$

where θ is the angle of a given facet from horizontal, and $a(\theta)$ is the distribution of surface slopes (Hapke, 1984). Alternatively, it can be measured in terms of the RMS surface slope (Spencer, 1990). This then allows comparison of results derived using different surface roughness representations (e.g., craters of different opening angles and fractional coverages, or different Gaussian random surfaces: Davidsson et al., 2015), and comparison against roughness measured by other means. It has been demonstrated that different roughness representations produce similar degrees of thermal infrared beaming when they have the same degree of roughness measured in terms of these values (Spencer, 1990; Emery et al., 1998; Lagerros, 1998; Rozitis

and Green, 2011).

5. DATA ANALYSIS USING A TPM

5.1. Thermal infrared spectro-photometry

Physical properties than can be derived from TPM fits to disk-integrated thermal observations include the diameter, geometric albedo, thermal inertia and roughness. In practically all cases, the absolute visual magnitude H is known, establishing a link between D and p_V and reducing the number of TPM fit parameters by one:

$$D(\text{km}) = 1329 \, p_V^{-1/2} \, 10^{-H/5}, \qquad (11)$$

(Fowler and Chillemi, 1992; Vilenius et al., 2012). Frequently, the rotational phase during the thermal observations is not sufficiently well known and has to be fitted to the thermal data (e.g., Harris et al., 2005; Alí-Lagoa et al., 2014). In some cases, TPMs can be used to constrain the orientation of the spin vector of an asteroid, with λ_p and β_p treated as free parameters (as demonstrated e.g., by Müller et al., 2013, 2012, note that in the case of 101955 Bennu the radar-constrained pole solution was not yet known). Moreover, Müller et al. (2014b) successfully performed a TPM analysis of an asteroid (99942 Apophis) in a non-principal axis rotation state for the first time.

The thermal effects of thermal inertia and surface roughness are difficult to tell apart. A commonly used approach is to use four different roughness models corresponding to no, low, medium, and high roughness, with each model leading to a different thermal-inertia fit (Mueller, 2007; Delbo and Tanga, 2009); frequently, the scatter between these four solutions accounts for the bulk of the uncertainty in thermal inertia. However, in some lucky cases, data do allow the effects of roughness and thermal inertia to be disentangled. This requires good wavelength coverage straddling the thermal emission peak and good coverage in solar phase angle, such that both the morning and afternoon sides of the asteroid are seen. See Fig. 6 for an illustration.

The best-fitting model parameters are those that minimize χ^2. Their uncertainty range is spanned by the values that lead to χ^2 within a specified threshold of the best fit, depending on the number of free fit parameters. Ideally, the reduced χ^2 of the best fit should be around unity. However, due to systematic uncertainties introduced in thermal infrared observations (e.g., flux offsets between different instruments), and/or in the thermophysical modeling, it is not uncommon to get large reduced χ^2 values. Large χ^2 values are also obtained when the assumed shape model differs significantly from the asteroid's true shape (Rozitis and Green, 2014). In particular, if the spatial extent of the shape model's z-axis is wrong, this can lead to diameter determinations that are inconsistent with radar observations (e.g., for 2002 NY_{40} and (308635) 2005 YU_{55} in Müller et al., 2004, 2013, respectively), and/or two different thermal inertia determinations (e.g., the two different results produced for (101955) Bennu by Emery et al., 2014; Müller et al.,
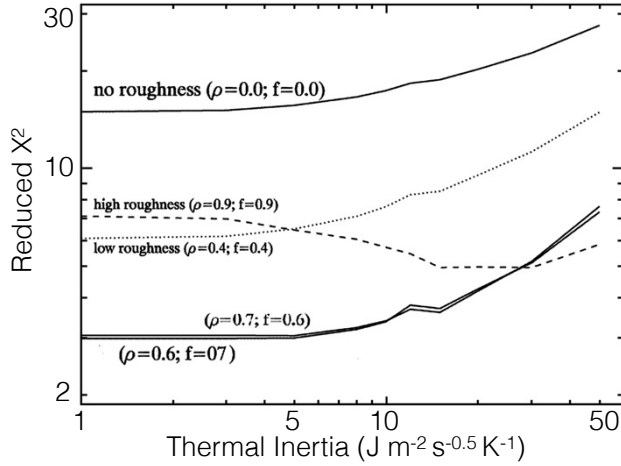
Fig. 6.— (21) Lutetia: a TPM fit that allows surface roughness to be constrained. The quantity ρ here is not the bulk density of the body, but it is the r.m.s. of the slopes on the surface. It is related to the ratio between the diameter and the depth of spherical section craters (Lagerros, 1998) in this particular case. f is the areal fraction of each facet covered with craters. From O'Rourke et al. (2012).

2012). In some works, the asteroid shape model has also been optimized during the thermophysical fitting to resolve inconsistencies with radar observations (e.g., (1862) Apollo and (1620) Geographos in Rozitis et al., 2013; Rozitis and Green, 2014, respectively).

We remind the reader that the accuracy of the physical properties (in particular the value of Γ) of asteroids derived from TPM depends on the quality of the thermal infrared data, coverage in wavelength, phase, rotational, and aspect angle. The accuracy of the shape model and of the H and G values are also important (see e.g. Rozitis and Green, 2014). The derived thermal inertia value often depends on the assumed degree of roughness and it is usually affected by large errors (e.g. 50 or 100 %, see Tab. 2). Care must be used in accepting TPM solutions purely based on the goodness of fit (e.g. the value of the χ^2), as they can be dominated by one or few measurements with unreliable small errors or calibration offsets between measurements from different sources.

5.2. Thermal Inertia and Thermal Conductivity

As asteroids rotate, the day-night cycle causes cyclic temperature variations that are controlled by the thermal inertia (defined by Eq. 4) of the soil and the rotation rate of the body. In the limit of vanishing thermal inertia, the surface temperature would be in instantaneous equilibrium with the incoming flux, depending only on the solar incidence angle (as long as self heating can be neglected); surface temperatures would peak at local noon and would be zero at night. In reality, thermal conduction into and from the sub-soil causes a certain thermal memory, referred to as *thermal inertia*. This smoothens the diurnal temperature profile,

leads to non-zero night-side temperatures, and causes the surface temperature to peak on the afternoon side, as shown in Fig. 2, thereby causing the Yarkovsky effect (§ 5.8).

The mass density ρ, the specific heat capacity c, and the thermal conductivity κ, and correspondingly Γ itself, must be thought of as effective values representative of the depth range sampled by the heat wave, which is typically in the few-cm range. In turn, thermal-inertia values inform us about the physical properties of the top few centimeters of the surface, not about bulk properties of the object.

As will be discussed below (§ 6.5), ρ and c of an asteroid surface can plausibly vary within a factor of several, while plausible values of κ span a range of more than 4 orders of magnitude. It is therefore not unjustified to convert from Γ to κ and back using reference values for ρ and c (note that Yarkovsky/YORP models tend to phrase the thermal-conduction problem in units of κ, while TPMs tend to be formulated in units of Γ, which is the observable quantity).

Importantly, the κ of finely powdered lunar regolith is 3 orders of magnitude lower than that of compact rock (compact metal is even more conductive by another order of magnitude). This is because radiative thermal conduction between regolith grains is significantly less efficient than phononic heat transfer within a grain. A fine regolith, an aggregate of very small grains, is a poor thermal conductor and displays a low Γ. Thermal inertia can therefore be used to infer the presence or absence of thermally insulating powdered surface material. In extension, thermal inertia can be used as a proxy of regolith grain size. The required calibration under Mars conditions (where the tenuous atmosphere enhances thermal conduction within pores compared to a vacuum) was obtained by Presley and Christensen (1997a,b) and used in the analysis of thermal-inertia maps of Mars (see Mellon et al., 2000; Putzig and Mellon, 2007). Similar progress in asteroid science was slowed down by the lack of corresponding laboratory measurements under vacuum conditions (but see below for recent lab measurements of meteorites). However, Gundlach and Blum (2013) provided a calibration relation based on heat-transfer modeling in a granular medium.

5.3. Temperature dependence of thermal inertia

Thermal inertia is a function of temperature (Keihm, 1984), chiefly because the thermal conductivity is. In general, for a lunar-like regolith the thermal conductivity is given by:

$$\kappa = \kappa_b + 4\sigma r_p T^3 \qquad (12)$$

where κ_b is the solid-state thermal conductivity (heat conduction by phonons) and r_p is the radius of the pores of the regolith. The term proportional to T^3 is due to the heat conduction by photons. Equation 12 is often written in the form $\kappa = \kappa_0(1 + \chi T^3)$ (e.g., Vasavada et al., 1999). Note that κ_b is itself a function of T (Opeil et al., 2010). There is extensive literature on the T-dependence of the conductivity of lunar regolith (e.g., Vasavada et al., 1999, and references therein). A theoretical description of the temperature de-

pendence of κ in regoliths is given by Gundlach and Blum (2013).

Asteroid TPMs typically neglect the temperature dependence of Γ. This is uncritical for typical remote observations, which are dominated by the warm sunlit hemisphere (see Fig. 7 and Capria et al., 2014; Vasavada et al., 2012). In the analysis of highly spatially resolved observations, however, the temperature dependence must be considered, certainly when analyzing night-time observations on low-Γ asteroids. Note that for temperature-dependent κ, Eq. 2 must be used instead of Eq. 3 (see, e.g., Capria et al., 2014).
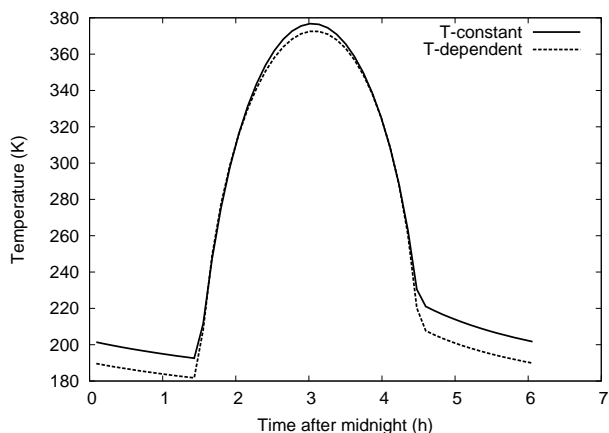

Fig. 7.— Diurnal temperature curves at the equator of an asteroid with A=0.1, P=6h, ϵ=1.0 at a heliocentric distance of 1.0 au. Solid curve: constant thermal conductivity κ=0.02 W K^{-1} m^{-1}. Dashed-curved: temperature-dependent heat conductivity $\kappa = 10^{-2}(1 + 0.5(T/250)^3)$ W K^{-1} m^{-1}.

Caution must be exercised when comparing thermal-inertia results obtained at different heliocentric distances r, i.e., at different temperatures. All other things being equal, $T^4 \propto r^{-2}$. Assuming that the T^3 term dominates in Eq. 12, the thermal inertia of a test object scales with (see also Mueller et al., 2010):

$$\Gamma \propto \sqrt{\kappa} \propto T^{3/2} \propto r^{-3/4}. \qquad (13)$$

5.4. Binary Asteroid TPM

A rather direct determination of thermal inertia can be obtained by observing the thermal response to eclipses and their aftermath, allowing one to see temperature changes in real time. Such observations have been carried out for planetary satellites such as the Galilean satellites (Morrison and Cruikshank, 1973), and our Moon (Pettit, 1940; Shorthill, 1973; Lawson et al., 2003; Lucey, 2000; Fountain et al., 1976). Mueller et al. (2010) report the first thermal observations of eclipse events in a binary Trojan asteroid system, (617) Patroclus, where one component casts shadow on the other while not blocking the line of sight toward the observer.

The thermophysical modeling of eclipse events is relatively straightforward, assuming the system is in a tidally locked rotation state typical of evolved binary systems. In that case, the components' spin rates match one another, and their spin axes are aligned with that of the mutual orbit. The system is therefore at rest in a co-rotating frame and can be modeled like a single object with a non-convex (disjoint!) global shape. Eclipse effects are fully captured, provided that shadowing between facets is accounted for. The two hemispheres that face one another can, in principle, exchange heat radiatively. This is negligible for typical binary systems, however.

As discussed above, the thermal effects of roughness and thermal inertia can be hard to disentangle. In the case of eclipse measurements, which happen at essentially constant solar phase angle, the effect of surface roughness is much less of a confounding factor. This is because the variation in the thermal signal is dominated by the temperature change induced by the passing shadow, which is a strong function of thermal inertia.

It must be kept in mind that the duration of an eclipse event is short compared to the rotation period. The eclipse-induced heat wave therefore probes the subsoil less deeply than the diurnal heat wave does (the typical heat penetration depth is given by Eq. 5 with P equal to the duration of the eclipse event). A depth dependence of thermal inertia (see § 6.6) could manifest itself in different thermal-inertia determinations using the two different measurement methods.

5.5. Thermal-infrared interferometry

Interferometric observations of asteroids in the thermal infrared measure the spatial distribution of the thermal emission along different directions on the plane of sky, thereby constraining the distribution in surface temperature and hence thermal inertia and roughness. Provided the asteroid shape is known, interferometry can be used to break the aforementioned degeneracy between thermal inertia and roughness from a single-epoch observation (Matter et al., 2011, 2013). Interferometry also allows a precise determination of the size of an asteroid (Delbo et al., 2009).

Spatial resolutions between 20 and 200 milli-arcseconds can be obtained from the ground (see Durech et al., 2015, for a review and future perspectives of the application of this technique).

While for the determination of asteroid sizes and shapes from interferometric observations in the thermal infrared, simple thermal models can be used (Delbo et al., 2009; Carry et al., 2015), a TPM was utilized to calculate interferometric visibilities of asteroids in the thermal infrared for the observations of (41) Daphne (Matter et al., 2011) and (16) Psyche (Matter et al., 2013).

Mid-infrared interferometric instruments measure the total flux and the visibility of a source, the latter being related to the intensity of the Fourier Transform (FT) of the spatial flux distribution along the interferometer's baseline projected on the plane of sky. Thus, the data analysis procedure consisted in generating images of the thermal infrared emission of the asteroids at different wavelengths as viewed by the interferometer and then in obtaining the model visi-

bility and flux for each image. The former is related to the FT of the image, the latter is simply the sum of the pixels. The free parameters of the TPM (size, thermal inertia value and roughness) are adjusted in order to minimize the distance between the disk integrated flux and visibility of the model, and the corresponding observed quantities (see Matter et al., 2011, 2013; Durech et al., 2015, for further information). Some results from these observational programs are discussed in § 6 and in the chapter by Durech et al. (2015).

5.6. Disk-resolved data and retrieval of temperatures

The availability of disk-resolved thermal-infrared observation has been increasingly steadily over the years: the ESA mission *Rosetta* performed two successful flybys to the asteroids (2867) Steins (in 2008) and (21) Lutetia (in 2010) (Barucci et al., 2015). In 2011, the NASA mission *Dawn* began its one-year orbiting of (4) Vesta (Russell et al., 2012); Dawn is reaching (1) Ceres at the time of writing. JAXA's *Hayabusa II* sample-return mission will map its target asteroid (162173) 1999 JU$_3$ using the thermal infrared imager (TIR) aboard the spacecraft (Okada et al., 2013); NASA's *OSIRIS-REx* mission and its thermal spectrometer OTES will do likewise for its target asteroid (101955) Bennu (in 2018-2019). These data can be used to derive surface-temperature maps, from which maps of thermal inertia and roughness can be derived.

Three different methods are used to measure surface temperatures from orbiting spacecraft: bolometry, mid-infrared spectroscopy, and near-infrared spectroscopy. In the following, we will elaborate on the challenges posed by these different methods, and on their dependence on spectral features, surface roughness, illumination geometry, and viewing geometry.

Bolometers measure thermal flux within a broad bandpass in the infrared, approximating the integral of the Planck function, $U = \sigma T_e^4$ (e.g., Kieffer et al., 1977; Paige et al., 2010). The temperature derived in this way (**effective temperature**) is directly relevant to the energy balance on the surface. Since the bolometric flux is spectrally integrated, the resulting temperature is fairly insensitive to spectral emissivity variations, as long as the bolometric emissivity (weighted spectrally averaged emissivity) is known or can be reasonably approximated.

Temperatures derived from mid-infrared spectrometry, on the other hand, are typically **brightness temperatures,** i.e., the temperature of a black body emitting at the wavelength in question. It is generally assumed that at some wavelength, the spectral emissivity is very close to 1.0, and the brightness temperature at this wavelength is taken as the surface temperature.

Spacecraft sent to asteroids (and/or comets) have more commonly been instrumented with near-infrared spectrometers (e.g., $\lambda < 5$ μm) rather than mid-infrared spectrometers. The long-wavelength ends of these spectrometers often extend into the range where thermal emission dominates

the measured flux (for the daytime surface temperatures of most asteroids). At these wavelengths, one cannot assume that the emissivity is close to 1.0. It is therefore not practical to derive brightness temperatures. Instead, the **color temperature** is derived, that is the temperature of a black body that emits with the same spectral shape. Such derivations have to separate temperature from spectral emissivity. The problem is under-constrained (N+1 unknowns, but only N data points), so there is no deterministic solution. Spectral emissivities for fine-grained silicates trend in the same direction as the blackbody curve, so it would be very easy to mistake spectral emissivity variations for different temperatures. The most statistically rigorous approach that has been applied to separating temperature and spectral emissivity in the $3 - 5$ μm region is that of Keihm et al. (2012) and Tosi et al. (2014) for Rosetta/VIRTIS data of Lutetia and Dawn/VIR data of Vesta.

Temperatures thus measured represent an average temperature in the field of view of a given pixel: illuminated hot zones and shadowed colder parts will both contribute. They do not directly correspond to a physical temperature of the soil; rather, they depend sensitively on the observation and illumination geometry (see Rozitis and Green, 2011, in particular their Fig. 9), especially in the case of large illumination angles.

Microwave spectrometers such as MIRO (Gulkis et al., 2007) can provide both day and nightside thermal flux measurements. At sub-mm, mm, and longer wavelengths, asteroid soils become moderately transparent. Subsurface layers contribute significantly to the observable thermal emission, thus providing information on the subsurface temperature. Observable fluxes depend on the subsurface temperature profile, weighted by the wavelength-dependent electrical skin depths, so both a thermal and an electrical model are required to interpret such data (Keihm et al., 2012).

We remind here that thermal infrared fluxes should be used as input data for TPMs and not (effective, color, or brightness) temperatures derived from radiometric methods, because of their dependence on illumination and observation angles !

5.7. Sample-return missions

Space agencies across the planet are developing space missions to asteroids, notably sample-return missions to primitive (C and B type) near-Earth asteroids: Hayabusa-2, was launched by JAXA towards (162173) 1999 JU$_3$ on December 3, 2014, and OSIRIS-REx is to be launched by NASA in 2016 (Lauretta et al., 2012). A good understanding of the expected thermal environment, which is governed by thermal inertia, is a key factor in planning spacecraft operations on or near asteroid surfaces. E.g., OSIRIS-REx is constrained to sampling a regolith not hotter than 350 K, severely constraining the choice of the latitude of the sample selection area on the body, the local time, and the arrival date on the asteroid.

Both Hayabusa-2 and OSIRIS-REx are required to take

regolith samples from the asteroid surface back to Earth. Obviously, this requires that regolith be present in the first place, which needs to be ascertained by means of ground-based thermal-inertia measurements. The sampling mechanism of OSIRIS-REx, in particular, requires relatively fine (cm-sized or smaller) regolith.

5.8. Accurate Yarkovsky and YORP modeling from TPMs

Scattered and thermally emitted photons carry momentum. Any asymmetry in the distribution of outgoing photons can, after averaging over an orbital period, impart a net recoil force (Yarkovsky effect) and/or a net torque (YORP effect) on the asteroid. Both effects are more noticeable as the object gets smaller. For small enough objects, the orbits can be significantly affected by the Yarkovsky effect, and their rotation state by YORP (Bottke et al., 2006; Vokrouhlický et al., 2015).

The strength of the Yarkovsky effect is strongly influenced by thermal inertia (Bottke et al., 2006, and references therein) and by the degree of surface roughness (Rozitis and Green, 2012). However, the strength and sign of the YORP rotational acceleration on an asteroid is independent of thermal inertia (Čapek and Vokrouhlický, 2004), but it is highly sensitive to the shadowing (Breiter et al., 2009), self-heating (Rozitis and Green, 2013), and surface roughness effects (Rozitis and Green, 2013) that are incorporated in thermophysical models.

Accurate calculations of the instantaneous recoil forces and torques require an accurate calculation of surface temperatures as afforded by TPMs; Rozitis and Green (2012, 2013) report on such models. Other than on thermal inertia, the Yarkovsky-induced orbital drift depends on the bulk mass density. Therefore, Yarkovsky measurements combined with thermal-inertia measurements can be used to infer the elusive mass density (Mommert et al., 2014b,a; Rozitis and Green, 2014; Rozitis et al., 2014, 2013). In the case of (101955) Bennu, the uncertainties in published values of thermal inertia (Emery et al., 2014) and measured Yarkovsky drift (Chesley et al., 2014) are so small that the accuracy of the inferred mass density rivals that of the expected in-situ spacecraft result (1260 ± 70 kg m^{-3}, i.e., a nominal uncertainty of only 6%). Rozitis et al. (2014) derived the bulk density of (29075) 1950 DA and used it to reveal the presence of cohesive forces stabilizing the object against the centrifugal force.

In turn, the measured Yarkovsky drift can be used to infer constraints on thermal inertia. This was first done by Chesley et al. (2003) studying the Yarkovsky effect on (6489) Golevka and by Bottke et al. (2001) studying the Koronis family in the main asteroid belt; both studies revealed thermal inertias consistent with expectations based on the observed correlation between thermal inertia and diameter (see § 6.2).

Whilst the YORP effect is highly sensitive to small-scale uncertainties in an asteroid's shape model (Statler, 2009), it can be used to place constraints on the internal bulk density distribution of an asteroid (Scheeres and Gaskell, 2008). For instance, Lowry et al. (2014) explain the YORP detection on (25143) Itokawa, which was opposite in sign to that predicted, by Itokawa's two lobes having substantially different bulk densities. However, unaccounted lateral heat conduction in thermal skin depth sized rocks could also explain, at least partially, this opposite sign result (Golubov and Krugly, 2012).

6. LATEST RESULTS FROM TPMs

In the *Asteroid III* era, thermal properties were known for only a few asteroids, i.e., (1) Ceres, (2) Pallas, (3) Juno, (4) Vesta, (532) Herculina from Müller and Lagerros (2002), and (433) Eros from Lebofsky and Rieke (1979). Since then, the number of asteroids with known thermal properties has increased steadily. We count 59 minor bodies with known value of Γ (see Tab. 2). Of these, 16 are near-Earth asteroids (NEAs), 27 main-belt asteroids (MBAs), 4 Jupiter Trojans, 5 Centaurs, and 7 trans-Neptunian objects (TNOs).

These classes of objects present very different physical properties such as sizes, regolith grain size, average value of the thermal inertia, and composition. Other important differences are their average surface temperature due to their very different heliocentric distances and orbital elements. The illumination and observation geometry are also diverse for different classes of objects. For instance, for TNOs and MBAs the phase angle of observation from Earth and Earth-like orbits is typically between a few and a few tens of degrees, respectively. On the other hand, NEAs can be observed under a much wider range of phase angles than can approach hundred degrees and more Müller (see also 2002). A special care should be used in these cases to explicitly calculate the heat diffusion in craters instead of using the approximation of Eq. 9.

6.1. Ground truth from space missions to asteroids

A number of asteroids have been, or will be, visited by spacecraft, providing ground-truth for the application of TPMs to remote-sensing thermal-infrared data.

(21) Lutetia: based on ground-based data and a TPM, Mueller et al. (2006) measured Lutetia's effective diameter and p_V to within a few percent of the later Rosetta result (Sierks et al., 2011). Their thermal-inertia constraint ($\Gamma < 50$ J m^{-2}s$^{-1/2}$K^{-1}) was refined by O'Rourke et al. (2012) based on the Rosetta shape model and more than 70 thermal-infrared observations obtained from the ground, *Spitzer*, *Akari*, and *Herschel*: $\Gamma = 5$ J m^{-2}s$^{-1/2}$K^{-1}with a high degree of surface roughness. Keihm et al. (2012) used MIRO aboard Rosetta to obtain a surface thermal inertia $\lesssim 30$ J m^{-2}s$^{-1/2}$K^{-1}. The low thermal inertia can be explained by a surface covered in fine regolith; Gundlach and Blum (2013) infer a regolith grain size of about 200 μm. The study of the morphology of craters by Vincent et al. (2012) indicates abundant, thick (600 m), and very fine re-

TABLE 2

PUBLISED THERMAL INERTIA VALUES

Number	Name	D (km)	Δ_D (km)	Γ (SI)	Δ_Γ (SI)	Tax	r (au)	Ref.	Number	Name	D (km)	Δ_D (km)	Γ (SI)	Δ_Γ (SI)	Tax	r (au)	Ref.
1	Ceres	923	20	10	10	C	2.767	1	1620	Geographos	5.04	0.07	340	120	S	1.1	12
2	Pallas	544	43	10	10	B	2.772	1	1862	Apollo	1.55	0.07	140	100	Q	1.0	13
3	Juno	234	11	5	5	S	2.671	1	2060	Chiron	142	10	4	4	B/Cb	8-15	14
4	Vesta	525	1	20	15	V	2.3	2	2060	Chiron	218	20	5	5	B/Cb	13	15
16	Psyche	244	25	125	40	M	2.7	3	2363	Cebriones	82	5	7	7	D	5.2	16
21	Lutetia	96	1	5	5	M	2.8	4	2867	Steins	4.92	0.4	150	60	E	2.1	17
22	Kalliope	167	17	125	125	M	2.3	5	2867	Steins	5.2	1	210	30	E	2.1	18
32	Pomona	85	1	70	50	S	2.8	6	8405	Asbolus	66	4	5	5	-	7.9	19
41	Daphne	202	7	25	25	Ch	2.1	7	3063	Makhaon	116	4	15	15	D	4.7	16
44	Nysa	81	1	120	40	E	2.5	6	10199	Chariklo	236	12	1	1	D	13	14
45	Eugenia	198	20	45	45	C	2.6	5	10199	Chariklo	248	18	16	14	D	13	13
87	Sylvia	300	30	70	60	P	2.7	5	25143	Itokawa	0.32	0.03	700	100	S	1.1	8
107	Camilla	245	25	25	10	P	3.2	5	25143	Itokawa	0.320	0.029	700	200	S	1.1	20
110	Lydia	93.5	3.5	135	65	M	2.9	6	29075	1950 DA	1.30	0.13	24	20	M	1.7	21
115	Thyra	92	2	62	38	S	2.5	6	33342	1998 WT$_{24}$	0.35	0.04	200	100	E	1.0	8
121	Hermione	220	22	30	25	Ch	2.9	5	50000	Quaoar	1082	67	6	4	-	43	15
130	Elektra	197	20	30	30	Ch	2.9	5	54509	YORP	0.092	0.010	700	500	S	1.1	8
277	Elvira	38	2	250	150	S	2.6	6	55565	2002 AW$_{197}$	700	50	10	10	-	47	22
283	Emma	135	14	105	100	P	2.6	5	90377	Sedna	995	80	0.1	0.1	-	87	23
306	Unitas	56	1	180	80	S	2.2	6	90482	Orcus	968	63	1	1	-	48	13
382	Dodona	75	1	80	65	M	2.6	6	99942	Apophis	0.375	0.014	600	300	Sq	1.05	24
433	Eros	17.8	1	150	50	S	1.6	8	101955	Bennu	0.495	0.015	650	300	B	1.1	25
532	Herculina	203	14	10	10	S	2.772	1	101955	Bennu	0.49	0.02	310	70	B	1.1	26
617	Patroclus	106	11	20	15	P	5.9	9	136108	Haumea	1240	70	0.3	0.2	-	51	27
694	Ekard	109.5	1.5	120	20	-	1.8	6	162173	1999 JU$_3$	0.87	0.03	400	200	C	1.4	28
720	Bohlinia	41	1	135	65	S	2.9	6	175706	1996 FG$_3$	1.71	0.07	120	50	C	1.4	29
956	Elisa	10.4	0.8	90	60	-	1.8	10	208996	2003 AZ$_{84}$	480	20	1.2	0.6	-	45	27
1173	Anchises	136	15	50	20	P	5.0	11	308635	2005 YU$_{55}$	0.306	0.006	575	225	C	1.0	30
1580	Betulia	4.57	0.46	180	50	C	1.1	8	341843	2008 EV$_5$	0.370	0.006	450	60	C	1.0	31

References: [1] Müller and Lagerros (1998), [2] Leyrat et al. (2012), [3] Matter et al. (2013), [4] O'Rourke et al. (2012), [5] Marchis et al. (2012), [6] Delbo and Tanga (2009), [7] Matter et al. (2011), [8] Mueller (2007), [9] Mueller et al. (2010), [10] Lim et al. (2011), [11] Horner et al. (2012), [12] Rozitis and Green (2014), [13] Rozitis et al. (2013), [14] Groussin et al. (2004), [15] Fornasier et al. (2013), [16] Fernández et al. (2003), [17] Lamy et al. (2008), [18] Leyrat et al. (2011), [19] Fernández et al. (2002), [20] Müller et al. (2014a), [21] Rozitis et al. (2014), [22] Cruikshank et al. (2005), [23] Pál et al. (2012), [24] Müller et al. (2014b), [25] Müller et al. (2012), [26] Emery et al. (2014), [27] Lellouch et al. (2013), [28] Müller et al. (2011), [29] Wolters et al. (2011), [30] Müller et al. (2013), [31] Alí-Lagoa et al. (2014), Note: for Ceres, Pallas, Juno, and Herculina r is assumed equal to the semimajor asxis of the orbit.

golith, confirming the TPM results.

(433) Eros was studied by the NASA NEAR-Shoemaker space mission that allowed determination of the shape and size of this asteroid (mean radius of 8.46 km with a mean error of 16 m; Thomas et al., 2002). Mueller (2007) performed a TPM analysis of the ground-based thermal infrared data by Harris and Davies (1999), obtaining a best-fit diameter of 17.8 km that is within 5% of the Thomas et al. (2002) result of 16.9 km, and Γ in the range 100 - 200 J m^{-2}s$^{-1/2}$K^{-1}. The latter value, in agreement with TPM results of Lebofsky and Rieke (1979), implies coarser surface regolith than that on the Moon and larger asteroids (see, e.g., Mueller, 2007; Delbo et al., 2007). From the value of Γ of Mueller (2007), Gundlach and Blum (2013) calculated a 1-3 mm typical regolith grain size for Eros. Optical images of the NEAR-Schoemaker landing site at a resolution of about 1 cm/pixel (Veverka et al., 2001) show very smooth areas at the scale of the camera spatial resolution (Fig. 8), likely implying mm or sub-mm grain size regolith, consistent with TPM results.

(25143) Itokawa physical properties were derived *in-situ* by the JAXA sample-return mission Hayabusa, allowing us to compare the size, albedo and regolith nature derived from the TPMs with spacecraft results. Müller et al. (2014a) show an agreement within 2% between the size and the geometric visible albedo inferred from TPM analysis of thermal-infrared data and the value of the corresponding parameters from Hayabusa data. The TPM thermal inertia value for Itokawa is around 750 J m^{-2}s$^{-1/2}$K^{-1}, significantly higher than the value of our Moon (about 50 J m^{-2}s$^{-1/2}$K^{-1}) and of other large main belt asteroids including (21) Lutetia, implying a coarser regolith on this small NEA. The corresponding average regolith grain size according to Gundlach and Blum (2013) is $\sim$ 2 cm. Hayabusa observations from the optical navigation camera (ONC-T), obtained during the descent of the spacecraft to the "Muses Sea" region of the asteroid, reveal similar grain sizes, at a spatial resolution of up to 6 mm/pixel. In particular, Yano et al. (2006) describe "Muses Sea" as composed of numerous size-sorted granular materials ranging from several centimeters to subcentimeter scales. Itokawa's regolith material can be classified as "gravel", larger than submillimeter regolith powders filling in ponds on (433) Eros (Fig. 8).

It is worth pointing out, however, that "Muses Sea" is not representative of Itokawa's surface as a whole. Rather, it was selected as a touchdown site because, in earlier Hayabusa imaging, it appeared as particularly smooth (minimizing operational danger for the spacecraft upon touchdown) and apparently regolith rich (maximizing the chance of sampling regolith). Grain sizes measured at "Muses Sea" are therefore lower limits on typical grain sizes rather than values typical for the surface as a whole.

6.2. Thermal inertia of large and small asteroids

An inverse correlation between Γ and D was noticed by Delbo et al. (2007), then updated Delbo and Tanga (2009)
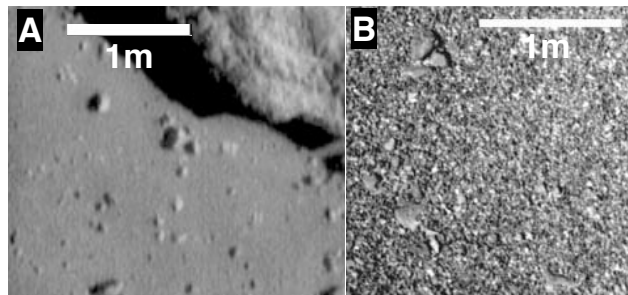

Fig. 8.— Higher Γ-values correspond to coarser regoliths. (A) Close-up image of (433) Eros from the NASA *NEAR Shoemaker* mission reveals coarse regolith with grain size in the mm-range (adapted from Veverka et al., 2001). The value of Γ is $\sim$150 J m^{-2}s$^{-1/2}$K^{-1} for Eros. (B) Image from the JAXA *Hayabusa* mission (from Yano et al., 2006) of the surface of (25143) Itokawa displaying gravel-like regolith. The value of Γ is $\sim$750 J m^{-2}s$^{-1/2}$K^{-1} for Itokawa.

and Capria et al. (2014). This supported the intuitive view that large asteroids have, over many hundreds of millions of years, developed substantial insulating regolith layers, responsible for the low values of their surface thermal inertia. On the other hand, much smaller bodies, with shorter collisional lifetimes (Marchi et al., 2006; Bottke et al., 2005, and references therein), have less regolith, and or larger regolith grains (less mature regolith), and therefore display a larger thermal inertia.

In the light of the recently published values of Γ (Tab. 2), said inversion correlation between Γ and D is less clear, in particular, when the values of the thermal inertia are temperature corrected (Fig. 9). However, the Γ vs D distribution of $D > 100$ km (large) asteroids is different than that of $D < 100$ km (small) asteroids. Small asteroids typically have higher Γ-values than large asteroids, which present a large scatter of Γ-values, ranging from a few to a few hundreds J m^{-2}s$^{-1/2}$K^{-1}. This is a clear indication of a diverse regolith nature amongst these large bodies. A shortage of low Γ values for small asteroids is also clear, with the notable exception of 1950 DA, which has an anomalously low Γ-value compared to other NEAs of similar size (Rozitis et al., 2014).

Fig. 9 also shows previously unnoticed high-thermal-inertia C types, maybe related to CR carbonaceous chondrites, which contain abundant metal phases. We also note that all E types in our sample appear to have a size-independent thermal inertia.

6.3. Very low Γ-values

We also note that the some of the C-complex outer main-belt asteroids and Jupiter Trojans have very low thermal inertia in the range between a few and a few tens of J m^{-2}s$^{-1/2}$K^{-1}. In order to reduce the thermal inertia of a material by at least one order of magnitude (from the lowest measured thermal inertia of a meteorite, $\sim$650 J m^{-2}s$^{-1/2}$K^{-1} at 200 K (Opeil et al., 2010), to the typical values for these
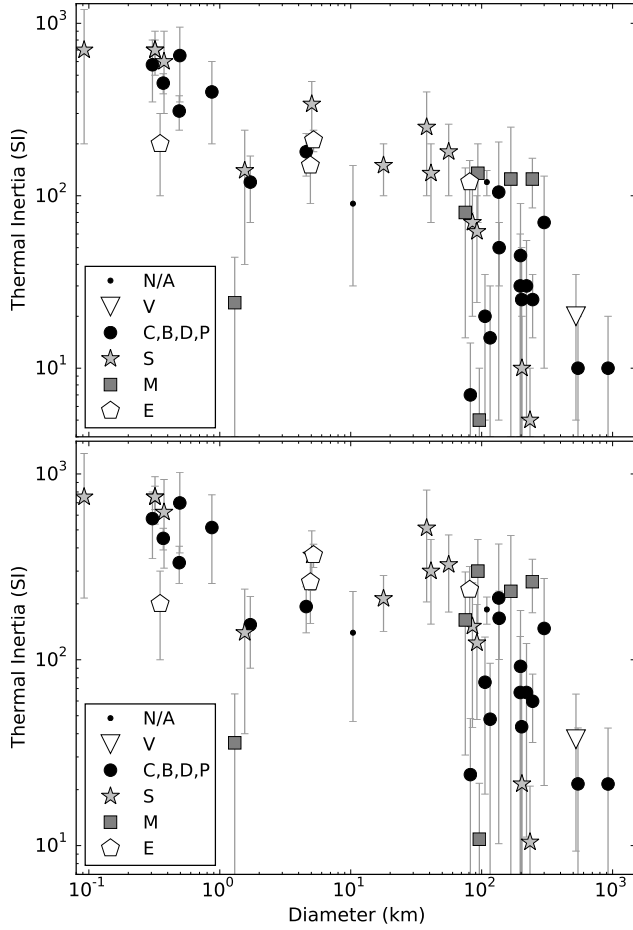
Fig. 9.— Γ values vs. D from Tab. 2 for different taxonomic types (see key). Top plot: original measurements, bottom plot: Γ corrected to 1 au heliocentric distance for temperature dependent thermal inertia assuming Eq. 13 and the heliocentric distance at the time of thermal infrared observations reported in Tab. 2. Trojans, Centaurs and trans-Neptunian objects are not displayed.

large asteroids (Tab. 2 and Fig. 9), a very large porosity (>90%) of the first few mm of the regolith is required (Vernazza et al., 2012). This is consistent with the discovery that emission features in the mid-infrared domain (7–25 μm, Fig. 4) are rather universal among large asteroids and Jupiter Trojans (Vernazza et al., 2012), and that said features can be reproduced in the laboratory by suspending meteorite and/or mineral powder (with grain sizes < 30 μm) in IR-transparent KBr (potassium bromide) powder (Vernazza et al., 2012). As KBr is not supposed to be present on the surfaces of these minor bodies, regolith grains must be "suspended" in void space likely due to cohesive forces and/or dust levitation. On the other hand, radar data indicate a significant porosity (40-50 %) of the first ~1 m of regolith (Magri et al., 2001; Vernazza et al., 2012), indicating decreasing porosity with increasing depth (see Fig. 5 of Vernazza et al., 2012, for a regolith schematics).

6.4. Average thermal inertia of asteroid populations

As described before, the thermal inertia of an asteroid can be directly derived by comparing measurements of its thermal-infrared emission to model fluxes generated by means of a TPM. Typically, more than one observation epoch is required to derive the thermal inertia, in order to "see" the thermal emission from different parts of the asteroid's diurnal temperature distribution. Unfortunately, the large majority of minor bodies for which we have thermal-infrared observations have been observed at a single epoch and/or information about their gross shape and pole orientation is not available, precluding the use of TPMs. However, if one assumes the thermal inertia to be roughly constant within a population of asteroids (e.g., NEAs) one can use observations of different asteroids under non-identical illumination and viewing geometries, as if they were from a unique object. Delbo et al. (2003) noted that qualitative information about the average thermal properties of a sample of NEAs could be obtained from the distribution of the η-values of the sample as a function of the phase angle, α. Delbo et al. (2007) and Lellouch et al. (2013) developed a rigorous statistical inversion method, based on the comparison of the distributions of published NEATM η-values vs α, or vs. r with that of a synthetic population of asteroids generated through a TPM, using realistic distributions of the input TPM parameters such as the rotation period, the aspect angle etc. Delbo et al. (2007) found that the average thermal inertia value for km-sized NEAs is around 200 J m^{-2}s$^{-1/2}$K^{-1}. The average thermal inertia of binary NEAs is higher than that of non-binary NEAs, possibly indicating a regolith-depriving mechanism for the formation of these bodies (Delbo et al., 2011). The same authors also found that NEAs with slow rotational periods (P >10 h) have higher-than-average thermal inertia. From a sample of 85 Centaurs and trans-Neptunian objects observed with Spitzer/MIPS and Herschel/PACS, Lellouch et al. (2013) found that surface roughness is significant, a mean thermal inertia $\Gamma = 2.5 \pm 0.5$ J m^{-2}s$^{-1/2}$K^{-1}, and a trend toward decreasing Γ with increasing heliocentric distance. The thermal inertias derived by Lellouch et al. (2013) are 2-3 orders of magnitude lower than expected for compact ices, and generally lower than on Saturn's satellites or in the Pluto/Charon system. These results are suggestive of highly porous surfaces.

6.5. Relevant astronomical and laboratory data

Physical interpretations of thermal-inertia estimates depend strongly on laboratory and ground-truth measurements of relevant material properties. While in the *Asteroid III* era, we based interpretation of thermal inertia on Earth analog materials, in the last few years laboratory measurements were performed on asteroid analog materials, i.e., meteorites. Meteorite grain densities range from ~2800 kg m^{-3} for CM carbonaceous chondrites to ~3700 kg m^{-3} for enstatite chondrites (Consolmagno et al., 2006; Macke et al., 2010, 2011a,b). Heat capacities have been measured

for a wide sampling of meteorites by Consolmagno et al. (2013), who find that values for stony meteorites are between 450 and 550 J kg^{-2} K^{-1}, whereas C for irons tends to be smaller (330 – 380 J kg^{-2} K^{-1}). Opeil et al. (2012, 2010) present thermal conductivity measurements of stony meteorites, finding values of 0.5 W K^{-1} m^{-1} for the carbonaceous chondrite Cold Bokkeveld to 5.5 W K^{-1} m^{-1} for the enstatite chondrite Pillistfer. Their one iron meteorite sample has a κ of 22.4 W K^{-1} m^{-1}. They also find a linear correlation between and the inverse of the porosity, from which Opeil et al. (2012) conclude that the measured κ of the samples is controlled more by micro-fractures than by composition.

Grain size and packing, more than compositional heterogeneity, are responsible for different thermal inertias of different surfaces. This also explains why TPMs are capable of deriving asteroid physical parameters independently of the asteroid mineralogy. Conduction between grains is limited by the area of the grain contact (Piqueux and Christensen, 2009b,a). As grain size decreases to diameters less than about a thermal skin depth (few cm on most asteroids), conduction is more and more limited (e.g., Presley and Christensen, 1997b). On bodies with atmospheres, conduction through the air in pores can often efficiently transport heat. On airless bodies, however, radiation between grains, which is not very efficient, particularly at low T (e.g., Gundlach and Blum, 2012), is the only alternative to conduction across contacts (Fig. 10). Considering these two modes of energy transport and their dependence on grain size, Gundlach and Blum (2013) developed an analytical approach for determining grain size from thermal inertia measurements. They incorporated the measurements of material properties of meteorites measured above along with results of their own laboratory of heat transport in dusty layers. Additional laboratory measurements of conductivities of powdered meteorites under high vacuum would be valuable for more precise interpretation of asteroid thermal inertias.

The classic opportunity for ground-truth thermal measurements came with the Apollo missions. Astronauts on Apollo 15 and 17 carried out bore-hole style temperature measurements to depths of 1.4 m below the surface on Apollo 15 and 2.3 m below the surface on Apollo 17 (Langeseth and Keihm, 1977; Vaniman et al., 1991). Thermal conductivity of about 0.001 W K^{-1} m^{-1} was found in the top 2 to 3 cm of the lunar regolith, increasing to about 0.01 W K^{-1} m^{-1} over the next few cm, then to values as high as 2 W K^{-1} m^{-1} deeper into the surface where the regolith appears to have been very compacted (Langeseth and Keihm, 1977). Low thermal inertias derived from remote thermal infrared measurements (e.g. Wesselink, 1948b; Vasavada et al., 2012) agree with the very low κ in the topmost few cm of the lunar surface, and the Apollo measurements provide the necessary ground-truth for interpreting such low thermal inertias as very fine-grained, "fluffy" regolith. These measurements fostered, for instance, development of detailed models of lunar regolith (Keihm, 1984). Detailed
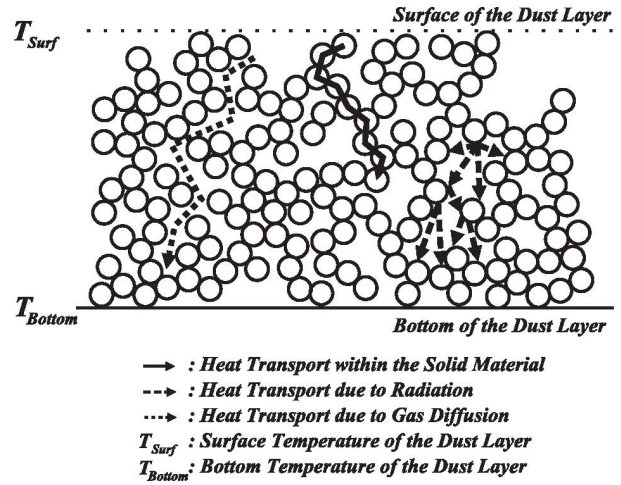

Fig. 10.— Diagram of the modes of heat transport in regoliths. On airless bodies, heat can flow by conduction through grain boundaries (solid line) or by radiation between grains (dashed line). The dotted line showing transport by gas diffusion is not relevant to asteroid surfaces. From Gundlach and Blum (2012).

thermal infrared observations and thermal models of the lunar regolith allows today estimating the subsurface rock abundance (e.g., Bandfield et al., 2011), allowing geological studies of the regolith production rate.

6.6. Dependence of Γ with depth

The depth dependence of typical asteroid regolith properties is poorly constrained at this point, which is why physical constants are typically assumed to be constant with depth. MIRO observations of (21) Lutetia, however, showed the existence of a top layer with $\Gamma < 30$ J m^{-2}s$^{-1/2}$K^{-1}, while the thermal inertia of subsurface material appears to increase with depth much like on the Moon (Keihm et al., 2012).

6.7. Infrared limb brightening

Recent modeling and observations show that, contrary to expectation, the flux enhancement measured in disk-integrated observations of the sunlit side of an asteroid (e.g., Lebofsky et al., 1986) is dominated by limb surfaces rather than the subsolar region (Rozitis and Green, 2011; Keihm et al., 2012). This suggests that for the sunlit side of an asteroid, sunlit surfaces directly facing the observer in situations where they would not be if the surface was a smooth flat one are more important than mutual self-heating between interfacing facets raising their temperatures. Figure 9 of Rozitis and Green (2011) pictures this effect for a Gaussian random surface during sunrise viewed from different directions. The thermal flux observed is enhanced when viewing hot sunlit surfaces (i.e., Sun behind the observer), and is reduced when viewing cold shadowed surfaces (i.e., Sun in front of the observer).

Jakosky et al. (1990) also studied the directional thermal emission of Earth-based lava flows exhibiting macroscopic

15

roughness. They found that enhancements in thermal emission were caused by viewing hot sunlit sides of rocks and reductions were caused by viewing cold shadowed sides of rocks. This agrees precisely with the model and adds further evidence that thermal infrared beaming is caused by macroscopic roughness rather than microscopic roughness.

The effect of limb brightening has also been measured from disk-resolved thermal infrared data (<5 μm) acquired during sunrise on the nucleus of the comet 9P/Tempel 1 by the *Deep Impact* NASA space mission (Davidsson et al., 2013), and from VIRTIS and MIRO measurements of the asteroid (21) Lutetia (Keihm et al., 2012).

6.8. Asteroid thermal inertia maps

Disk-resolved thermal infrared observations, in the range between $4.5 – 5.1$ μm, were provided by the instrument VIR (De Sanctis et al., 2012) on board of the NASA DAWN (Russell et al., 2012) spacecraft (Capria et al., 2014, and references therein). Form TPM analysis of VIR measurements, Capria et al. (2014) obtained a map of the roughness and the thermal inertia of Vesta. The average thermal inertia of Vesta is 30 ± 10 J m^{-2}s$^{-1/2}$K^{-1}, which is in good agreement with the values found by ground-based observations (Müller and Lagerros, 1998; Chamberlain et al., 2007; Leyrat et al., 2012). The best analog is probably the surface of the Moon, as depicted by Vasavada et al. (2012) and Bandfield et al. (2011): a surface whose thermal response is determined by a widespread layer of dust and regolith with different grain sizes and density increasing toward the interior. Exposed rocks are probably scarce or even absent. Capria et al. (2014) also show that Vesta cannot be considered uniform from the point of view of thermal properties. In particular, they found that the thermal inertia spatial distribution follows the global surface exposure age distribution, as determined by crater counting in Raymond et al. (2011), with higher thermal inertia displayed by younger terrains and lower thermal inertia in older soils.

Capria et al. (2014) also found higher-than-average thermal inertia terrain units located in low-albedo regions that contain highest abundance of OH, as determined by the 2.8 μm band depth (De Sanctis et al., 2012). These terrains are associated with the dark material, thought to be delivered by carbonaceous chondrite like asteroids that have impacted Vesta at low velocity. Note that in general (carbonaceous chondrites) have lower densities and lower thermal conductivity (Opeil et al., 2010) than basaltic material, which constitute the average Vestan terrain. This consideration would point to a lower thermal inertia rather than a higher one, as observed on Vesta. Capria et al. (2014) conclude that the factor controlling the thermal inertia in these areas could be the degree of compaction of the uppermost surface layers, which is higher than in other parts of the surface.

6.9. Thermal inertia of metal-rich regoliths

In principle, the composition of the regolith and not only its average grain size and the degree of compaction also affects the thermal inertia of the soil (Gundlach and Blum, 2013). For instance iron meteorites have a higher thermal conductivity than ordinary and carbonaceous chondrites (Opeil et al., 2010). We thus expect that a metal iron rich regolith displays a higher thermal inertia than a soil poor of this component. Harris and Drube (2014) compared values of the NEATM η-parameter derived from WISE data with asteroid taxonomic classifications and radar data, and showed that the η-value appears to be a useful indicator of asteroids containing metal. Matter et al. (2013) performed interferometric observations with MIDI of the ESO-VLTI in thermal infrared of (16) Psyche and showed that Psyche has a low surface roughness and a thermal inertia value around 120 ± 40 J m^{-2}s$^{-1/2}$K^{-1}, which is one of the higher values for an asteroid of the size of Psyche (~ 200 km). This higher than average thermal inertia supports the evidence of a metal-rich surface for this body.

7. EFFECTS OF TEMPERATURES ON THE SURFACE OF ASTEROIDS

7.1. Thermal cracking

The surface temperature of asteroids follows a diurnal cycle (see Fig. 2) with typically dramatic temperature changes as the Sun rises or sets. The resulting, repeated thermal stress can produce cumulative damage on surface material due to opening and extension of microscopic cracks. This phenomenon is known as *thermal fatigue* (Delbo et al., 2014).

Growing cracks can lead to rock break-up when the number of temperature cycles is large enough. For typical asteroid properties, this process is a very effective mechanism for comminuting rocks and to form fresh regolith (Delbo et al., 2014). For cm-sized rocks on an asteroid 1 au from the Sun, thermal fragmentation is at least an order of magnitude faster than comminution by micrometeoroid impacts, the only regolith-production mechanism previously considered relevant (Hörz and Cintala, 1997; Hoerz et al., 1975).

The efficiency of thermal fragmentation is dominated by the amplitude of the temperature cycles and by the temperature change rate (Hall and André, 2001), which in turn depend on heliocentric distance, rotation period, and the surface thermal inertia. The rate of thermal fragmentation increases with decreasing perihelion distance: at 0.14 au from the Sun, thermal fragmentation may erode asteroids such as (3200) Phaethon and produce the Geminids (Jewitt and Li, 2010), whereas in the outer Main Belt this process might be irrelevant. Thermal fragmentation of surface boulders is claimed by Dombard et al. (2010) to be source of fine regolith in the so-called "ponds" on the asteroid (433) Eros. Production of fresh regolith originating in thermal fatigue fragmentation may be an important process for the rejuvenation of the surfaces of near-Earth asteroids (Delbo et al., 2014).

Thermal cracking is reported on other bodies, too: on Earth, particularly in super-arid environments (Hall, 1999; Hall and André, 2001), on the Moon (Levi, 1973; Duen-

nebier and Sutton, 1974), Mercury (Molaro and Byrne, 2012), Mars (Viles et al., 2010), and on meteorites (Levi, 1973). Moreover, Tambovtseva and Shestakova (1999) suggest that thermal cracking could be an important process in the fragmentation and splitting of kilometer-sized comets while in the inner solar system. Furthermore, Čapek and Vokrouhlický (2010) initially proposed that slowly rotating meteoroids or meteoroids that have spin vector pointing towards the sun can be broken up by thermal cracking. In a further development of their model, Čapek and Vokrouhlický (2012) showed that as the meteoroid approaches the Sun, the stresses first exceed the material strength at the surface and create a fractured layer. If inter-molecular forces (e.g., Rozitis et al., 2014) are able to retain the surface layer, despite the competing effects of thermal lifting and centrifugal forces, the particulate surface layer is able to thermally shield the core, preventing any further damage by thermal stresses.

7.2. Sun-driven heating of near-Earth asteroids and meteoroids

It is known that heating processes can affect the physical properties of asteroids and their fragments, the meteorites (see, e.g., Keil, 2000).

Internal heating due to the decay of short-lived radionuclides was considered early on (Grimm and McSween, 1993). Marchi et al. (2009) discuss close approaches to the Sun as an additional surface-altering heating mechanism. In the present near-Earth asteroid population, the fraction of bodies with relatively small perihelion (q) is very small: about 1/2, 1/10, and 1/100 of the population of currently known near-Earth objects (11,000 as of the time of writing) have a perihelion distance below 1, 0.5, and 0.25 au, where maximum temperature are exceeding 400, 550, and 780 K, respectively (see Fig. 11). However, dynamical simulations show that a much larger fraction of asteroids had small perihelion distances for some time, hence experiencing episodes of strong heating in their past (Marchi et al., 2009). For instance, the asteroid 2004 LG was approaching the Sun to within only ∼5.6 solar radii some 3 ky ago, and its surface was baked at temperatures of 2500 K (Vokrouhlický and Nesvorný, 2012).

Solar heating has a penetration depth of typically a few cm (see Eq. 5 and Spencer et al., 1989). Organic components found on meteorites break up at temperatures as low as 300–670 K (see Fig. 11 and Kebukawa et al., 2010; Frost et al., 2000; Huang et al., 1994), thus solar heating can remove these components from asteroid surfaces.

7.3. Thermal metamorphism of meteorites

Radiative heating from the Sun has been invoked as a mechanism for the thermal metamorphism of metamorphic CK carbonaceous chondrites (Chaumard et al., 2012). The matrix of these chondrites shows textures consistent with a transient thermal event during which temperatures rose between 550 and 950 K. The inferred duration of these events
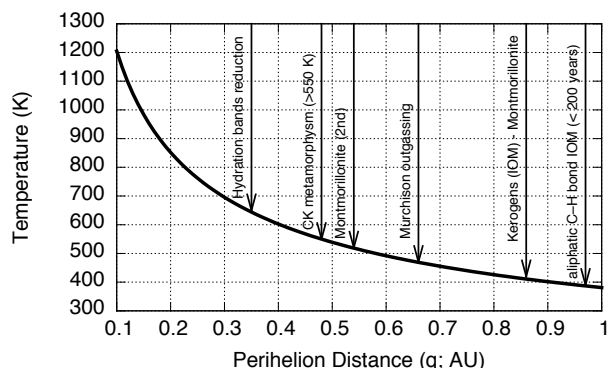

Fig. 11.— Surface temperature of an asteroid or meteoroid as a function of the distance from the Sun. Vertical arrows indicate the threshold temperature for the thermal alteration/desiccation for a variety of chemical compounds discussed in the text (see Delbo and Michel, 2011, and references therein for further information). The temperature range for thermal metamorphism of the CK chondrites is from Chaumard et al. (2012).

is of the order of days to years, much longer than the time scale of shock events but shorter than the time scale for heating by the decay of radiogenic species such as ^{26}Al (e.g., Kallemeyn et al., 1991).

7.4. Subsurface ice sublimation

Observational evidence for the presence of ice on asteroid surfaces stems from the discovery of main belt comets (MBCs; Hsieh and Jewitt, 2006), the localized release of water vapor from the surface of (1) Ceres (Küppers et al., 2014), and the detection of spectroscopic signatures interpreted as water ice frost on the surface of (24) Themis (Rivkin and Emery, 2010; Campins et al., 2010) and of (65) Cybele (Licandro et al., 2011).

The lifetime of ices on the surface and in the subsurface depends strongly on temperature. TPMs have been used to estimate these temperatures. This requires a modification of the "classical" TPM as presented in section 4, such that heat conduction is coupled with gas diffusion (Schorghofer, 2008; Capria et al., 2012; Prialnik and Rosenberg, 2009). The referenced models assume a spherical shape. As for the interior structure, Capria et al. (2012); Prialnik and Rosenberg (2009) assume a comet-like structure, i.e., an intimate mixture of ice and dust throughout the entire body, while Schorghofer (2008) consider an ice layer underneath a rocky regolith cover. Sublimation of ice and the transport of water molecules through the fine-grained regolith is modeled in all cases.

All authors agree that water ice exposed on asteroid surfaces sublimates completely on timescales much shorter than the age of the Solar System. Therefore, asteroid surfaces were expected to be devoid of water ice, contrary to the observational evidence quoted above. However, water ice can be stable over 4.5 Gy in the shallow subsurface, at a depth of ∼1–10 m. In particular, Fanale and Salvail (1989) showed that ice could have survived in the subsurface at the

polar regions of Ceres. Large heliocentric distances, slow rotation, and a fine-grained regolith leading to low thermal conductivity and short molecular free path, all favor the stabilization of subsurface water ice (Schorghofer, 2008). The same authors conclude that rocky surfaces, in contrast to dusty surfaces, are rarely able to retain ice in the shallow subsurface.

To be observable on the surface, buried ice most be exposed. Campins et al. (2010) describe several plausible mechanisms such as impacts, recent change in the obliquity of the spin pole, and daily or orbital thermal pulses reaching a subsurface ice layer.

8.   FUTURE CHALLENGES FOR TPMs

The *Spitzer* and *WISE* telescopes have opened a new era of asteroid thermal-infrared observations and the exploitation of their data through TPMs has just begun (e.g., Alí-Lagoa et al., 2014; Rozitis et al., 2014; Emery et al., 2014). At the moment, the limiting factor is the availability of accurate asteroid shape models. However, optical-wavelength all-sky surveys such as PanSTARRS, LSST, and Gaia are expected to produce enormous photometric data sets leading to thousands of asteroid models. We envision the availability of thousands of thermal-inertia values in some years from now, enabling more statistically robust studies of thermal inertia as a function of asteroid size, spectral class, albedo, rotation period, etc.

For instance, the distribution of Γ within asteroid families will be crucial in the search of evidence of asteroid differentiation: asteroid formation models and meteorite studies suggest that hundreds of planetesimals experienced complete or partial differentiation. An asteroid family formed from the catastrophic disruption of such a differentiated asteroid should contain members corresponding to the crust, the mantle and the iron core. However, the observed spectra and albedos are very homogeneous across asteroid families. Thermal inertia might help in separating iron rich from iron poor family members, supposedly originating respectively from the core and mantle of the differentiated parent body (e.g., Matter et al., 2013; Harris and Drube, 2014).

At any size range, Fig. 9 shows an almost tenfold variability in thermal inertia, corresponding to difference in average regolith grain size of almost two orders of magnitude Gundlach and Blum (2013). For small near-Earth asteroids, this could be due to a combination of thermal cracking (Delbo et al., 2014), regolith motion (Murdoch et al., 2015), and cohesive forces (Rozitis et al., 2014). Faster rotation periods allow more thermal cycles, which then enhances thermal fracturing. It also encourages regolith to move towards the equator where the gravitational potential is at its lowest (Walsh et al., 2008). And for the extremely fast rotators, large boulders/rocks could be selectively lofted away, because they stick less well to the surface than smaller particles. For $D > 100$ km sized asteroids, Γ-values might be help to distinguish between primordial and more recently re-accumulated asteroids. The former had ~ 4 Gy of regolith evolution, the latter have a less developed and therefore coarser regolith.

The high-precision thermal-infrared data of WISE and Spitzer pose new challenges to TPMs, as model uncertainties are now comparable to the uncertainty of the measured flux. This will become even more important with the launch of the James Webb Space Telescope (JWST). In particular, the accuracy of the shape models might represent a limiting factor (e.g., Rozitis and Green, 2014). The next challenge will be to allow the TPM to optimize the asteroid shape. This seems to be possible as the infrared photometry is also sensitive to shape, provided good-quality thermal data are available (Durech et al., 2015).

New interferometric facilities, such as MATISSE, LBTI, and ALMA, will become available in the next years requiring TPMs to calculate precise disk-resolved thermal fluxes (Durech et al., 2015). The wavelengths of ALMA, similar to those of MIRO, will allow to measure the thermal-infrared radiation from the subsoil of asteroids, thus providing further information about how thermal inertia varies with depth.

Certainly, constraining roughness is one of the future challenges for TPMs. To do so from disk-integrated data requires a range of wavelengths and solar phase angles. Low phase angle measurements are enhanced by beaming whilst high phase angle measurements are reduced by beaming. In particular, shorter wavelengths are affected more than longer wavelengths.

Moreover, the future availability of precise sizes and cross sections of asteroids from stellar occultation timing (Tanga and Delbo, 2007), combined with shape information derived from lightcurve inversion (Durech et al., 2015) will allow to remove the need to constrain the object size from TPM analysis. Iinfrared fluxes will thus be converted into highly reliable thermal inertia and roughness values.

REFERENCES

Alí-Lagoa V., Lionni L., Delbo M., et al. (2014). Thermophysical properties of near-Earth asteroid (341843) 2008 EV5 from WISE data. *Astronomy & Astrophysics*, *561*, A45.

Bandfield J. L., Ghent R. R., Vasavada A. R., et al. (2011). Lunar surface rock abundance and regolith fines temperatures derived from LRO Diviner Radiometer data. *Journal of Geophysical Research*, *116*.

Barucci A. M., Fulchignoni M., Ji J., et al. (2015). The Steins, Lutetia, and Toutatis fly-bys. In *Asteroids IV*. this book.

Bottke W. F., Durda D. D., Nesvorný D., et al. (2005). The fossilized size distribution of the main asteroid belt. *Icarus*, *175*, 111–140.

Bottke W. F., Vokrouhlický D., Broz M., et al. (2001). Dynamical Spreading of Asteroid Families by the Yarkovsky Effect. *Science*, *294*, 1693–1696.

Bottke W. F. J., Vokrouhlický D., Rubincam D. P., et al. (2006). The Yarkovsky and Yorp Effects: Implications for Asteroid Dynamics. *Annual Review of Earth and Planetary Sciences*, *34*, 157–191.

Breiter S., Bartczak P., Czekaj M., et al. (2009). The YORP effect on 25143 Itokawa. *Astronomy & Astrophysics*, *507*, 1073–1081.

Buhl D., Welch W. J., and Rea D. G. (1968a). Anomalous Cooling of a Cratered Lunar Surface. *Journal of Geophysical Research*, *73*, 7593–7608.

Buhl D., Welch W. J., and Rea D. G. (1968b). Reradiation and Thermal Emission from Illuminated Craters on the Lunar Surface. *Journal of Geophysical Research*, *73*, 5281–5295.

Campins H., Hargrove K., Pinilla-Alonso N., et al. (2010). Water ice and organics on the surface of the asteroid 24 Themis. *Nature*, *464*, 1320–1321.

Čapek D. and Vokrouhlický D. (2004). The YORP effect with finite thermal conductivity. *Icarus*, *172*, 526–536.

Čapek D. and Vokrouhlický D. (2010). Thermal stresses in small meteoroids. *Astronomy and Astrophysics*, *519*, A75.

Čapek D. and Vokrouhlický D. (2012). Thermal stresses in small meteoroids. II. Effects of an insulating surface layer. *Astronomy & Astrophysics*, *539*, A25.

Capria M. T., Marchi S., De Sanctis M. C., et al. (2012). The activity of main belt comets. *Astronomy & Astrophysics*, *537*, A71.

Capria M. T., Tosi F., De Sanctis M. C., et al. (2014). Vesta surface thermal properties map. *Geophysical Research Letters*, *41*, 1438–1443.

Carry B. (2012). Density of asteroids. *Planetary and Space Science*, *73*, 98–118.

Carry B., Matter A., Scheirich P., et al. (2015). The small binary asteroid (939) Isberga. *Icarus*, *248*, 516–525.

Chamberlain M. A., Lovell A. J., and Sykes M. V. (2007). Submillimeter lightcurves of Vesta. *Icarus*, *192*, 448–459.

Chamberlain M. A., Lovell A. J., and Sykes M. V. (2009). Submillimeter photometry and lightcurves of Ceres and other large asteroids. *Icarus*, *202*, 487–501.

Chaumard N., Devouard B., Delbo M., et al. (2012). Radiative heating of carbonaceous near-Earth objects as a cause of thermal metamorphism for CK chondrites. *Icarus*, *220*, 65–73.

Chesley S. R., Farnocchia D., Nolan M. C., et al. (2014). Orbit and bulk density of the OSIRIS-REx target Asteroid (101955) Bennu. *Icarus*, *235*, 5–22.

Chesley S. R., Ostro S. J., Vokrouhlický D., et al. (2003). Direct Detection of the Yarkovsky Effect by Radar Ranging to Asteroid 6489 Golevka. *Science*, *302*, 1739–1742.

Consolmagno G. J., Macke R. J., Rochette P., et al. (2006). Density, magnetic susceptibility, and the characterization of ordinary chondrite falls and showers. *Meteoritics & Planetary Science*, *41*, 331–342.

Consolmagno G. J., Schaefer M. W., Schaefer B. E., et al. (2013). The measurement of meteorite heat capacity at low temperatures using liquid nitrogen vaporization. *Planetary and Space Science*, *87*, 146–156.

Cruikshank D. P., Stansberry J. A., Emery J. P., et al. (2005). The High-Albedo Kuiper Belt Object (55565) 2002 AW197. *The Astrophysical Journal Letters*, *624*, L53–L56.

Davidsson B., Rickman H., Bandfield J. L., et al. (2015). *Interpretation of thermal emission. I. The effect of roughness for spatially resolved atmosphereless bodies*. Icarus (in press).

Davidsson B. J. R., Gutiérrez P. J., Groussin O., et al. (2013). Thermal inertia and surface roughness of Comet 9P/Tempel 1. *Icarus*, *224*, 154–171.

Davidsson B. J. R. and Rickman H. (2014). Surface roughness and three-dimensional heat conduction in thermophysical models. *Icarus*, *243*, 58–77.

De Sanctis M. C., Ammannito E., Capria M. T., et al. (2012). Spectroscopic Characterization of Mineralogy and Its Diversity Across Vesta. *Science*, *336*, 697–700.

Delbo M. (2004). The nature of near-Earth asteroids from the study of their thermal infrared emission. *PhD thesis*, pp. 1–210.

Delbo M., dell'Oro A., Harris A. W., et al. (2007). Thermal inertia of near-Earth asteroids and implications for the magnitude of the Yarkovsky effect. *Icarus*, *190*, 236–249.

Delbo M. and Harris A. W. (2002). Physical properties of near-Earth asteroids from thermal infrared observations and thermal modeling. *Meteoritics & Planetary Science*, *37*, 1929–1936.

Delbo M., Harris A. W., Binzel R. P., et al. (2003). Keck observations of near-Earth asteroids in the thermal infrared. *Icarus*, *166*, 116–130.

Delbo M., Libourel G., Wilkerson J., et al. (2014). Thermal fatigue as the origin of regolith on small asteroids. *Nature*, *508*, 233–236.

Delbo M., Ligori S., Matter A., et al. (2009). First VLTI-MIDI Direct Determinations of Asteroid Sizes. *The Astrophysical Journal*, *694*, 1228–1236.

Delbo M. and Michel P. (2011). Temperature History and Dynamical Evolution of (101955) 1999 RQ 36: A Potential Target for Sample Return from a Primitive Asteroid. *The Astrophysical Journal Letters*, *728*, L42.

Delbo M. and Tanga P. (2009). Thermal inertia of main belt asteroids smaller than 100 km from IRAS data. *Planetary and Space Science*, *57*, 259–265.

Delbo M., Walsh K., Mueller M., et al. (2011). The cool surfaces of binary near-Earth asteroids. *Icarus*, *212*, 138–148.

Dombard A. J., Barnouin O. S., Prockter L. M., et al. (2010). Boulders and ponds on the Asteroid 433 Eros. *Icarus*, *210*, 713–721.

Duennebier F. and Sutton G. H. (1974). Thermal moonquakes. *Journal of Geophysical Research*, *79*, 4351–4363.

Durech J., Carry B., Delbo M., et al. (2015). Asteroid Models from Multiple Data Sources. In *Asteroids IV*. University of Arizona Press, Tucson, AZ.

Emery J. P., Fernández Y. R., Kelley M. S. P., et al. (2014). Thermal infrared observations and thermophysical characterization of OSIRIS-REx target asteroid (101955) Bennu. *Icarus*, *234*, 17–35.

Emery J. P., Sprague A. L., Witteborn F. C., et al. (1998). Mercury: Thermal Modeling and Mid-infrared (5-12 μm) Observations. *Icarus*, *136*, 104–123.

Fanale F. P. and Salvail J. R. (1989). The water regime of asteroid (1) Ceres. *Icarus*, *82*, 97–110.

Fernández Y. R., Jewitt D. C., and Sheppard S. S. (2002). Thermal Properties of Centaurs Asbolus and Chiron. *The Astronomical Journal*, *123*, 1050–1055.

Fernández Y. R., Sheppard S. S., and Jewitt D. C. (2003). The Albedo Distribution of Jovian Trojan Asteroids. *The Astronomical Journal*, *126*, 1563–1574.

Fornasier S., Lellouch E., Müller T., et al. (2013). TNOs are Cool: A survey of the trans-Neptunian region. VIII. Combined Herschel PACS and SPIRE observations of nine bright targets at 70-500 μm. *Astronomy and Astrophysics*, *555*, A15.

Fountain W. F., Fountain J. A., Jones B. P., et al. (1976). Observational and theoretical temperatures for a total lunar eclipse. *The moon*, *15*, 421–437.

Fowler J. W. and Chillemi J. R. (1992). *IRAS asteroid data processing*. The IRAS Minor Planet Survey.

Frost R. L., Ruan H., Kloprogge J. T., et al. (2000). Dehydration and dehydroxylation of nontronites and ferruginous smectite. *Thermochimica Acta*, *346*, 63–72.

Giese B. and Kuehrt E. (1990). Theoretical interpretation of infrared measurements at Deimos in the framework of crater radiation. *Icarus*, *88*, 372–379.

Golubov O. and Krugly Y. N. (2012). Tangential Component of the YORP Effect. *The Astrophysical Journal Letters*, *752*, L11.

Grimm R. E. and McSween H. Y. (1993). Heliocentric zoning of the asteroid belt by aluminum-26 heating. *Science (ISSN 0036-8075)*, *259*, 653–655.

Groussin O., Lamy P., Fornasier S., et al. (2011). The properties of asteroid (2867) Steins from Spitzer Space Telescope observations and OSIRIS shape reconstruction. *Astronomy & Astrophysics*, *529*, A73.

Groussin O., Lamy P., and Jorda L. (2004). Properties of the nuclei of Centaurs Chiron and Chariklo. *Astronomy & Astrophysics*, *413*, 1163–1175.

Groussin O., Sunshine J. M., Feaga L. M., et al. (2013). The temperature, thermal inertia, roughness and color of the nuclei of Comets 103P/Hartley 2 and 9P/Tempel 1. *Icarus*, *222*, 580–594.

Gulkis S., Frerking M., Crovisier J., et al. (2007). MIRO: Microwave Instrument for Rosetta Orbiter. *Space Science Reviews*, *128*, 561–597.

Gundlach B. and Blum J. (2012). Outgassing of icy bodies in the Solar System - II: Heat transport in dry, porous surface dust layers. *Icarus*, *219*, 618–629.

Gundlach B. and Blum J. (2013). A new method to determine the grain size of planetary regolith. *Icarus*, *223*, 479–492.

Hall K. (1999). The role of thermal stress fatigue in the breakdown of rock in cold regions. *Geomorphology*, *31*, 47–63.

Hall K. and André M.-F. (2001). New insights into rock weathering from high-frequency rock temperature data: an Antarctic study of weathering by thermal stress. *Geomorphology*, *41*, 23–35.

Hanuš J., Brož M., Durech J., et al. (2013). An anisotropic distribution of spin vectors in asteroid families. *Astronomy & Astrophysics*, *559*, A134.

Hanuš J., Durech J., Brož M., et al. (2011). A study of asteroid pole-latitude distribution based on an extended set of shape models derived by the lightcurve inversion method. *Astronomy & Astrophysics*, *530*, 134.

Hapke B. (1984). Bidirectional reflectance spectroscopy. III - Correction for macroscopic roughness. *Icarus*, *59*, 41–59.

Hapke B. (1996). A model of radiative and conductive energy transfer in planetary regoliths. *Journal of Geophysical Research*, *101*, 16817–16832.

Harris A., Boslough M., Chapman C. R., et al. (2015). Asteroid Impacts and Modern Civilization: Can we Prevent a Catastrophe? In *Asteroids IV*. University of Arizona Press, Tucson, AZ.

Harris A. W. (1998). A Thermal Model for Near-Earth Asteroids. *Icarus*, *131*, 291–301.

Harris A. W. (2006). The surface properties of small asteroids from thermal-infrared observations. *Asteroids, Comets, Meteors. Proceedings IAU Symposium No. 229, 2005 D. Lazzaro, S. Ferraz-Mello & J.A. Fernandez, eds*, *229*, 449–463.

Harris A. W. and Davies J. K. (1999). Physical Characteristics of Near-Earth Asteroids from Thermal Infrared Spectrophotometry. *Icarus*, *142*, 464–475.

Harris A. W. and Drube L. (2014). How to Find Metal-rich Asteroids. *The Astrophysical Journal Letters*, *785*, L4.

Harris A. W. and Lagerros J. S. V. (2002). Asteroids in the Thermal Infrared. *Asteroids III, W. F. Bottke Jr., A. Cellino, P. Paolicchi, and R. P. Binzel (eds), University of Arizona Press, Tucson.*, pp. 205–218.

Harris A. W., Mueller M., Delbo M., et al. (2005). The surface properties of small asteroids: Peculiar Betulia—A case study. *Icarus*, *179*, 95–108.

Hoerz F., Schneider E., Gault D. E., et al. (1975). Catastrophic rupture of lunar rocks - A Monte Carlo simulation. *Lunar Science Institute*, *13*, 235–258.

Holsapple K. A. (2010). On YORP-induced spin deformations of asteroids. *Icarus*, *205*, 430–442.

Horner J., Müller T. G., and Lykawka P. S. (2012). (1173) Anchises - thermophysical and dynamical studies of a dynamically unstable Jovian Trojan. *Monthly Notices of the Royal Astronomical Society*, *423*, 2587–2596.

Hörz F. and Cintala M. (1997). Impact experiments related to the evolution of planetary regoliths. *Meteoritics & Planetary Science*, *32*, 179–209.

Hsieh H. H. and Jewitt D. (2006). A Population of Comets in the Main Asteroid Belt. *Science*, *312*, 561–563.

Huang W. L., Bassett W. A., and Wu T. C. (1994). Dehydration and hydration of montmorillonite at elevated temperatures and pressures monitored using synchrotron radiation. *American Mineralogist*, *79*, 683–691.

Huebner W. F., Benkhoff J., Capria M. T., et al. (2006). Heat and Gas Diffusion in Comet Nuclei. ISSI Scientific report SR-004, vol. 4. International Space Science Institute.

Jacobson S. A. and Scheeres D. J. (2011). Dynamics of rotationally fissioned asteroids: Source of observed small asteroid systems. *Icarus*, *214*, 161–178.

Jakosky B. M., Finiol G. W., and Henderson B. G. (1990). Directional variations in thermal emission from geologic surfaces. *Geophysical Research Letters*, *17*, 985–988.

Jewitt D., Hsieh H., and Agarwal J. (2015). The Active Asteroids. In *Asteroids IV*. University of Arizona Press, Tucson, AZ.

Jewitt D. and Li J. (2010). Activity in Geminid Parent (3200) Phaethon. *The Astronomical Journal*, *140*, 1519–1527.

Kallemeyn G. W., Rubin A. E., and Wasson J. T. (1991). The compositional classification of chondrites. V - The Karoonda (CK) group of carbonaceous chondrites. *Geochimica et Cosmochimica Acta*, *55*, 881–892.

Kebukawa Y., Nakashima S., and Zolensky M. E. (2010). Kinetics of organic matter degradation in the Murchison meteorite for the evaluation of parent-body temperature history. *Meteoritics & Planetary Science*, *45*, 99–113.

Keihm S., Kamp L., Gulkis S., et al. (2013). Reconciling main belt asteroid spectral flux density measurements with a self-consistent thermophysical model. *Icarus*, *226*, 1086–1102.

Keihm S., Tosi F., Kamp L., et al. (2012). Interpretation of combined infrared, submillimeter, and millimeter thermal flux data obtained during the Rosetta fly-by of Asteroid (21) Lutetia. *Icarus*, *221*, 395–404.

Keihm S. J. (1984). Interpretation of the lunar microwave brightness temperature spectrum - Feasibility of orbital heat flow mapping. *Icarus*, *60*, 568–589.

Keil K. (2000). Thermal alteration of asteroids: evidence from meteorites. *Planetary and Space Science*, *48*, 887–903.

Kieffer H. H., Martin T. Z., Peterfreund A. R., et al. (1977). Thermal and albedo mapping of Mars during the Viking primary mission. *Journal of Geophysical Research*, *82*, 4249–4291.

Küppers M., O'Rourke L., Bockelée-Morvan D., et al. (2014). Localized sources of water vapour on the dwarf planet (1) Ceres. *Nature*, *505*, 525–527.

Lagerros J. S. V. (1996a). Thermal physics of asteroids. I. Effects of shape, heat conduction and beaming. *Astronomy and Astrophysics*, *310*, 1011–1020.

Lagerros J. S. V. (1996b). Thermal physics of asteroids. II. Polarization of the thermal microwave emission from asteroids. *Astronomy & Astrophysics*, *315*, 625–632.

Lagerros J. S. V. (1997). Thermal physics of asteroids. III. Irregular shapes and albedo variegations. *Astronomy & Astrophysics*, *325*, 1226–1236.

Lagerros J. S. V. (1998). Thermal physics of asteroids. IV. Thermal infrared beaming. *Astronomy & Astrophysics*, *332*, 1123–1132.

Lamy P. L., Jorda L., Fornasier S., et al. (2008). Asteroid 2867 Steins. III. Spitzer Space Telescope observations, size determination, and thermal properties. *Astronomy & Astrophysics*, *487*, 1187–1193.

Langeseth M. G. and Keihm S. J. (1977). Lunar Heat-Flow Experiment. *NASA Technical Report NASA-CR-151619; CU-4-77*, pp. 1–289.

Lauretta D. S., Barucci M. A., Bierhaus E. B., et al. (2012). The OSIRIS-REx Mission — Sample Acquisition Strategy and Evidence for the Nature of Regolith on Asteroid (101955) 1999 RQ36. *Asteroids, Comets, Meteors. Proceedings IAU Symposium No. 229, 2005 D. Lazzaro, S. Ferraz-Mello & J.A. Fernandez, eds*, *1667*, 6291.

Lawson S. L. S. L., Rodger A. P. A. P., Bender S. C. S. C., et al. (2003). Multispectral thermal imager observations of the moon during total eclipse. *Lunar and Planetary Science XXXIV*.

Lebofsky L. A. and Rieke G. H. (1979). Thermal properties of 433 Eros. *Icarus*, *40*, 297–308.

Lebofsky L. A. and Spencer J. R. (1989). Radiometry and a thermal modeling of asteroids. In *Asteroids II*, pp. 128–147. University of Arizona Press, Tucson, AZ.

Lebofsky L. A., Sykes M. V., Tedesco E. F., et al. (1986). A refined 'standard' thermal model for asteroids based on observations of 1 Ceres and 2 Pallas. *Icarus*, *68*, 239–251.

Lellouch E., Santos-Sanz P., Lacerda P., et al. (2013). "TNOs are Cool": A survey of the trans-Neptunian region. IX. Thermal properties of Kuiper belt objects and Centaurs from combined Herschel and Spitzer observations. *Astronomy & Astrophysics*, *557*, 60.

Levi F. A. (1973). Thermal Fatigue: A Possible Source of Structural Modifications in Meteorites. *Meteoritics & Planetary Science*, *8*, 209–221.

Leyrat C., Barucci A., Mueller T., et al. (2012). Thermal properties of (4) Vesta derived from Herschel measurements. *Astronomy & Astrophysics*, *539*, A154.

Leyrat C., Coradini A., Erard S., et al. (2011). Thermal properties of the asteroid (2867) Steins as observed by VIRTIS/Rosetta. *Astronomy & Astrophysics*, *531*, A168.

Licandro J., Campins H., Kelley M., et al. (2011). (65) Cybele: detection of small silicate grains, water-ice, and organics. *Astronomy & Astrophysics*, *525*, A34.

Lim L. F., Emery J. P., and Moskovitz N. A. (2011). Mineralogy and thermal properties of V-type Asteroid 956 Elisa: Evidence for diogenitic material from the Spitzer IRS (5-35 μm) spectrum. *Icarus*, *213*, 510–523.

Lowry S. C., Weissman P. R., Duddy S. R., et al. (2014). The internal structure of asteroid (25143) Itokawa as revealed by detection of YORP spin-up. *Astronomy & Astrophysics*, *562*, A48.

Lucey P. G. (2000). Observations of the moon using the Air Force Maui Space Surveillance Complex. *Proc. SPIE Vol. 4091*, *4091*, 216–224.

Lucey P. G. (2006). Radiative transfer modeling of the effect of mineralogy on some empirical methods for estimating iron concentration from multispectral imaging of the Moon. *Journal of Geophysical Research*, *111*, 8003.

Macke R. J., BRITT D. T., and Consolmagno G. J. (2011a). Density, porosity, and magnetic susceptibility of achondritic meteorites. *Meteoritics & Planetary Science*, *46*, 311–326.

Macke R. J., Consolmagno G. J., and BRITT D. T. (2011b). Density, porosity, and magnetic susceptibility of carbonaceous chondrites. *Meteoritics & Planetary Science*, *46*, 1842–1862.

Macke R. J., Consolmagno G. J., BRITT D. T., et al. (2010). Enstatite chondrite density, magnetic susceptibility, and porosity. *Meteoritics & Planetary Science*, *45*, 1513–1526.

Magri C., Consolmagno G. J., Ostro S. J., et al. (2001). Radar constraints on asteroid regolith compositions using 433 Eros as ground truth. *Meteoritics & Planetary Science*, *36*, 1697–1709.

Mainzer A., Trilling D., and Usui F. (2015). Space-Based Infrared Studies of Asteroids. In *Asteroids IV*. University of Arizona Press, Tucson, AZ.

Marchi S., Delbo M., Morbidelli A., et al. (2009). Heating of near-Earth objects and meteoroids due to close approaches to the Sun. *Monthly Notices of the Royal Astronomical Society*, *400*, 147–153.

Marchi S., Paolicchi P., Lazzarin M., et al. (2006). A General Spectral Slope-Exposure Relation for S-Type Main Belt and Near-Earth Asteroids. *The Astronomical Journal*, *131*, 1138–1141.

Marchis F., Enriquez J. E., Emery J. P., et al. (2012). Multiple asteroid systems: Dimensions and thermal properties from Spitzer Space Telescope and ground-based observations. *Icarus*, *221*, 1130–1161.

Matter A., Delbo M., Carry B., et al. (2013). Evidence of a metal-rich surface for the Asteroid (16) Psyche from interferometric observations in the thermal infrared. *Icarus*, *226*, 419–427.

Matter A., Delbo M., Ligori S., et al. (2011). Determination of physical properties of the Asteroid (41) Daphne from interferometric observations in the thermal infrared. *Icarus*, *215*, 47–56.

McSween H. Y. J., Ghosh A., Grimm R. E., et al. (2002). Thermal Evolution Models of Asteroids. *Asteroids III, W. F. Bottke Jr., A. Cellino, P. Paolicchi, and R. P. Binzel (eds), University of Arizona Press, Tucson.*, pp. 559–571.

Mellon M. T., Jakosky B. M., Kieffer H. H., et al. (2000). High-Resolution Thermal Inertia Mapping from the Mars Global Surveyor Thermal Emission Spectrometer. *Icarus*, *148*, 437–455.

Molaro J. and Byrne S. (2012). Rates of temperature change of airless landscapes and implications for thermal stress weathering. *Journal of Geophysical Research*, *117*, 10011.

Mommert M., Farnocchia D., Hora J. L., et al. (2014a). Physical Properties of Near-Earth Asteroid 2011 MD. *The Astrophysical Journal Letters*, *789*, L22.

Mommert M., Hora J. L., Farnocchia D., et al. (2014b). Constraining the Physical Properties of Near-Earth Object 2009 BD. *The Astrophysical Journal*, *786*, 148.

Morrison D. and Cruikshank D. P. (1973). Thermal Properties of the Galilean Satellites. *Icarus*, *18*, 224–236.

Mueller M. (2007). *Surface Properties of Asteroids from Mid-Infrared Observations and Thermophysical Modeling*. PhD thesis, PhD thesis on arXiv.org.

Mueller M., Harris A. W., Bus S. J., et al. (2006). The size and albedo of Rosetta fly-by target 21 Lutetia from new IRTF measurements and thermal modeling. *Astronomy & Astrophysics*, *447*, 1153–1158.

Mueller M., Marchis F., Emery J. P., et al. (2010). Eclipsing binary Trojan asteroid Patroclus: Thermal inertia from Spitzer observations. *Icarus*, *205*, 505–515.

Müller T. G. (2002). Thermophysical analysis of infrared observations of asteroids. *Meteoritics & Planetary Science*, *37*, 1919–1928.

Müller T. G. and Barnes P. J. (2007). 3.2 mm lightcurve observations of (4) Vesta and (9) Metis with the Australia Telescope Compact Array. *Astronomy & Astrophysics*, *467*, 737–747.

Müller T. G., Durech J., Hasegawa S., et al. (2011). Thermophysical properties of 162173 (1999 JU3), a potential flyby and rendezvous target for interplanetary missions. *Astronomy and Astrophysics*, *525*, 145.

Müller T. G., Hasegawa S., and Usui F. (2014a). (25143) Itokawa: The power of radiometric techniques for the interpretation of remote thermal observations in the light of the Hayabusa rendezvous results*. *Publications of the Astronomical Society of Japan*, *66*, 52.

Müller T. G., Kiss C., Scheirich P., et al. (2014b). Thermal infrared observations of asteroid (99942) Apophis with Herschel. *Astronomy & Astrophysics*, *566*, A22.

Müller T. G. and Lagerros J. S. V. (1998). Asteroids as far-infrared photometric standards for ISOPHOT. *Astronomy & Astrophysics*, *338*, 340–352.

Müller T. G. and Lagerros J. S. V. (2002). Asteroids as calibration standards in the thermal infrared for space observatories. *Astronomy & Astrophysics*, *381*, 324–339.

Müller T. G., Miyata T., Kiss C., et al. (2013). Physical properties of asteroid 308635 (2005 YU55) derived from multi-instrument infrared observations during a very close Earth approach. *Astronomy & Astrophysics*, *558*, A97.

Müller T. G., O'Rourke L., Barucci A. M., et al. (2012). Physical properties of OSIRIS-REx target asteroid (101955) 1999 RQ36. Derived from Herschel, VLT/ VISIR, and Spitzer observations. *Astronomy & Astrophysics*, *548*, A36.

Müller T. G., Sterzik M. F., Schütz O., et al. (2004). Thermal infrared observations of near-Earth asteroid 2002 NY40. *Astronomy & Astrophysics*, *424*, 1075–1080.

Murdoch N., sanchez P., Schwartz S. R., et al. (2015). Asteroid Surface Geophysics. In *Asteroids IV*. University of Arizona Press, Tucson, AZ.

Okada T., Fukuhara T., Tanaka S., et al. (2013). Thermal-Infrared Imager TIR on Hayabusa2: Science and Instrumentation. *44th Lunar and Planetary Science Conference*, *44*, 1954.

Opeil C. P., Consolmagno G. J., and Britt D. T. (2010). The thermal conductivity of meteorites: New measurements and analysis. *Icarus*, *208*, 449–454.

Opeil C. P., Consolmagno G. J., Safarik D. J., et al. (2012). Stony meteorite thermal properties and their relationship with meteorite chemical and physical states. *Meteoritics & Planetary Science*, *47*, 319–329.

O'Rourke L., Müller T., Valtchanov I., et al. (2012). Thermal and shape properties of asteroid (21) Lutetia from Herschel observations around the Rosetta flyby. *Planetary and Space Science*, *66*, 192–199.

Paige D. A., Foote M. C., Greenhagen B. T., et al. (2010). The Lunar Reconnaissance Orbiter Diviner Lunar Radiometer Experiment. *Space Science Reviews*, *150*, 125–160.

Pál A., Kiss C., Müller T. G., et al. (2012). "TNOs are Cool": A survey of the trans-Neptunian region. VII. Size and surface characteristics of (90377) Sedna and 2010 EK139. *Astronomy and Astrophysics*, *541*, L6.

Pettit E. (1940). Radiation Measurements on the Eclipsed Moon. *Astrophysical Journal*, *91*, 408–421.

Pettit E. and Nicholson S. B. (1930). Lunar radiation and temperatures. *The Astrophysical Journal*, *71*, 102–135.

Piqueux S. and Christensen P. R. (2009a). A model of thermal conductivity for planetary soils: 1. Theory for unconsolidated soils. *Journal of Geophysical Research*, *114*, 9005.

Piqueux S. and Christensen P. R. (2009b). A model of thermal conductivity for planetary soils: 2. Theory for cemented soils. *Journal of Geophysical Research*, *114*, 9006.

Piqueux S. and Christensen P. R. (2011). Temperature-dependent thermal inertia of homogeneous Martian regolith. *Journal of Geophysical Research*, *116*, 7004.

Pravec P., Scheirich P., KUSNIRAK P., et al. (2006). Photometric survey of binary near-Earth asteroids. *Icarus*, *181*, 63–93.

Presley M. A. and Christensen P. R. (1997a). Thermal conductivity measurements of particulate materials 1. A review. *Journal of Geophysical Research*, *102*, 6535–6550.

Presley M. A. and Christensen P. R. (1997b). Thermal conductivity measurements of particulate materials 2. results. *Journal of Geophysical Research*, *102*, 6551–6566.

Prialnik D. and Rosenberg E. D. (2009). Can ice survive in main-belt comets? Long-term evolution models of comet 133P/Elst-Pizarro. *Monthly Notices of the Royal Astronomical Society (ISSN 0035-8711)*, *399*, L79–L83.

Putzig N. E. and Mellon M. T. (2007). Apparent thermal inertia and the surface heterogeneity of Mars. *Icarus*, *191*, 68–94.

Raymond C. A., Jaumann R., Nathues A., et al. (2011). The Dawn Topography Investigation. *Space Science Reviews*, *163*, 487–510.

Redman R. O., Feldman P. A., Matthews H. E., et al. (1992). Millimeter and submillimeter observations of the asteroid 4 Vesta. *Astronomical Journal (ISSN 0004-6256)*, *104*, 405–411.

Rivkin A. S. and Emery J. P. (2010). Detection of ice and organics on an asteroidal surface. *Nature*, *464*, 1322–1323.

Rozitis B., Duddy S. R., Green S. F., et al. (2013). A thermophysical analysis of the (1862) Apollo Yarkovsky and YORP effects. *Astronomy and Astrophysics*, *555*, A20.

Rozitis B. and Green S. F. (2011). Directional characteristics of thermal-infrared beaming from atmosphereless planetary surfaces - a new thermophysical model. *Monthly Notices of the Royal Astronomical Society*, *415*, 2042–2062.

Rozitis B. and Green S. F. (2012). The influence of rough surface thermal-infrared beaming on the Yarkovsky and YORP effects. *Monthly Notices of the Royal Astronomical Society*, *423*, 367–388.

Rozitis B. and Green S. F. (2013). The influence of global self-heating on the Yarkovsky and YORP effects. *Monthly Notices of the Royal Astronomical Society*, *433*, 603–621.

Rozitis B. and Green S. F. (2014). Physical characterisation of near-Earth asteroid (1620) Geographos. Reconciling radar and thermal-infrared observations. *Astronomy & Astrophysics*, *568*, A43.

Rozitis B., MacLennan E., and Emery J. P. (2014). Cohesive forces prevent the rotational breakup of rubble-pile asteroid (29075) 1950 DA. *Nature*, *512*, 174–176.

Russell C. T., Raymond C. A., Coradini A., et al. (2012). Dawn at Vesta: Testing the Protoplanetary Paradigm. *Science*, *336*, 684–686.

Scheeres D. J. (2007). Rotational fission of contact binary asteroids. *Icarus*, *189*, 370–385.

Scheeres D. J. and Gaskell R. W. (2008). Effect of density inhomogeneity on YORP: The case of Itokawa. *Icarus*, *198*, 125–129.

Schorghofer N. (2008). The Lifetime of Ice on Main Belt Asteroids. *The Astrophysical Journal*, *682*, 697–705.

Sexl R. U., Sexl H., Stremnitzer H., et al. (1971). The directional characteristics of lunar infrared radiation. *The moon*, *3*, 189–213.

Shorthill R. W. (1973). Infrared Atlas Charts of the Eclipsed Moon. *The moon*, *7*, 22–45.

Sierks H., Lamy P., Barbieri C., et al. (2011). Images of Asteroid 21 Lutetia: A Remnant Planetesimal from the Early Solar System. *Science*, *334*, 487–490.

Smith B. G. (1967). Lunar surface roughness: Shadowing and thermal emission. *Journal of Geophysical Research*.

Spencer J. R. (1990). A rough-surface thermophysical model for airless planets. *Icarus*, *83*, 27–38.

Spencer J. R., Lebofsky L. A., and Sykes M. V. (1989). Systematic biases in radiometric diameter determinations. *Icarus*, *78*, 337–354.

Statler T. S. (2009). Extreme sensitivity of the YORP effect to small-scale topography. *Icarus*, *202*, 502–513.

Tambovtseva L. V. and Shestakova L. i. (1999). Cometary splitting due to thermal stresses. *Planetary and Space Science*, *47*, 319–326.

Tanga P. and Delbo M. (2007). Asteroid occultations today and tomorrow: toward the GAIA era. *Astronomy and Astrophysics*, *474*, 1015–1022.

Thomas P. C., Joseph J., Carcich B., et al. (2002). Eros: Shape, Topography, and Slope Processes. *Icarus*, *155*, 18–37.

Tosi F., Capria M. T., De Sanctis M. C., et al. (2014). Thermal measurements of dark and bright surface features on Vesta as derived from Dawn/VIR. *Icarus*, *240*, 36–57.

Urquhart M. L. and Jakosky B. M. (1997). Lunar thermal emission and remote determination of surface properties. *Journal of Geophysical Research*, *102*, 10959–10970.

Vaniman D., Reddy R., Heiken G., et al. (1991). The Lunar Environment. In *Lunat Sourcebook* (Heiken G. H., Vaniman D., and French K. L., editors), pp. 27–60. Cambridge University Press., Cambridge, UK.

Vasavada A. R., Bandfield J. L., Greenhagen B. T., et al. (2012). Lunar equatorial surface temperatures and regolith properties from the Diviner Lunar Radiometer Experiment. *Journal of Geophysical Research*, *117*.

Vasavada A. R., Paige D. A., and Wood S. E. (1999). Near-Surface Temperatures on Mercury and the Moon and the Stability of Polar Ice Deposits. *Icarus*, *141*, 179–193.

Vernazza P., Delbo M., King P. L., et al. (2012). High surface porosity as the origin of emissivity features in asteroid spectra. *Icarus*, *221*, 1162–1172.

Veverka J., Farquhar B., Robinson M., et al. (2001). The landing of the NEAR-Shoemaker spacecraft on asteroid 433 Eros. *Nature*, *413*, 390–393.

Vilenius E., Kiss C., Mommert M., et al. (2012). "TNOs are Cool": A survey of the trans-Neptunian region. VI. Herschel/PACS observations and thermal modeling of 19 classical Kuiper belt objects. *Astronomy & Astrophysics*, *541*, A94.

Viles H., Ehlmann B., Wilson C. F., et al. (2010). Simulating weathering of basalt on Mars and Earth by thermal cycling. *Geophysical Research Letters*, *37*, 18201.

Vincent J.-B., Besse S., Marchi S., et al. (2012). Physical properties of craters on asteroid (21) Lutetia. *Planetary and Space Science*, *66*, 79–86.

Vokrouhlický D., Bottke W. F., Chesley S. R., et al. (2015). The Yarkovsky and YORP effects. In *Asteroids IV*. University of Arizona Press, Tucson, AZ.

Vokrouhlický D. and Nesvorný D. (2012). Sun-grazing orbit of the unusual near-Earth object 2004 LG. *Astronomy & Astrophysics*, *541*, A109.

Vokrouhlický D., Nesvorný D., and Bottke W. F. (2003). The vector alignments of asteroid spins by thermal torques. *Nature*, *425*, 147–151.

Walsh K. J., Richardson D. C., and Michel P. (2008). Rotational breakup as the origin of small binary asteroids. *Nature*, *454*, 188–191.

Wesselink A. J. (1948a). Heat conductivity and nature of the lunar surface material. *Bulletin of the Astronomical Institutes of the Netherlands*, *10*, 351–363.

Wesselink A. J. (1948b). Heat conductivity and nature of the lunar surface material. *Bulletin of the Astronomical Institutes of the Netherlands*, *10*, 351–363.

Winter D. F. and Krupp J. A. (1971). Directional characteristics of infrared emission from the moon. *The moon*, *2*, 279–292.

Wolters S. D. and Green S. F. (2009). Investigation of systematic bias in radiometric diameter determination of near-Earth asteroids: the night emission simulated thermal model (NESTM). *Monthly Notices of the Royal Astronomical Society*, *400*, 204–218.

Wolters S. D., Rozitis B., Duddy S. R., et al. (2011). Physical characterization of low delta-V asteroid (175706) 1996 FG3. *Monthly Notices of the Royal Astronomical Society*, *418*, 1246–1257.

Yano H., Kubota T., Miyamoto H., et al. (2006). Touchdown of the Hayabusa Spacecraft at the Muses Sea on Itokawa. *Science*, *312*, 1350–1353.